The Three Hundred project: dissecting the Fundamental Plane of galaxy clusters up to $z = 1$

Luis A. Díaz-García [1,2]★ Keiichi Umetsu [1], Elena Rasia,[3,4] Weiguang Cui [5]
and Massimo Meneghetti[6,7]

[1]*Academia Sinica Institute of Astronomy and Astrophysics (ASIAA), No. 1, Section 4, Roosevelt Road, Taipei 10617, Taiwan*
[2]*Instituto de Astrofísica de Andalucía (IAA-CSIC), PO Box 3004, E-18080 Granada, Spain*
[3]*INAF - Osservatorio Astronomico Trieste, via Tiepolo 11, I-34123 Trieste, Italy*
[4]*Institute of Fundamental Physics of the Universe, via Beirut 2, Grignano, I-34151 Trieste, Italy*
[5]*Institute for Astronomy, University of Edinburgh, Edinburgh EH9 3HJ, UK*
[6]*INAF - Osservatorio Astronomico di Bologna, via Ranzani 1, I-40127 Bologna, Italy*
[7]*INFN, Sezione di Bologna, viale Berti Pichat 6/2, I-40127 Bologna, Italy*

ABSTRACT

We perform a systematic study of the recently discovered Fundamental Plane of galaxy clusters (CFP) using ∼250 simulated clusters from The Three Hundred project, focusing on the stability of the plane against different temperature definitions and its dependence on the dynamical relaxation state of clusters. The CFP is characterized by $T \propto M_s^\alpha r_s^\beta$, defined with the gas temperature (T) and the characteristic halo scale radius and mass (r_s and M_s) assuming a Navarro–Frenk–White halo description. We explore two definitions of weighted temperatures, namely mass-weighted and spectroscopic-like temperatures, in three radial ranges. The Three Hundred project clusters at $z = 0$ lie on a thin plane whose parameters (α, β) and dispersion (0.015–0.030 dex) depend on the gas temperature definition. The CFP for mass-weighted temperatures is closer to the virial equilibrium expectation ($\alpha = 1$, $\beta = -1$) with a smaller dispersion. For gas temperatures measured within 500 h^{-1} kpc, the resulting CFP deviates the most from the virial expectation and shifts towards the similarity solution for a secondary infall model ($\alpha = 1.5$, $\beta = -2$). Independently of the temperature definition, we find that clusters at $z = 1$ and relaxed clusters form a CFP similar to the virial expectation, unlike disturbed clusters exhibiting stronger evolution. Only systems formed over the last 4 Gyr present a CFP that is closer to the similarity solution. All these findings are compatible with the CFP obtained for a Cluster Lensing And Supernova survey with *Hubble* subsample excluding the hottest clusters with $T_X > 12$ keV.

Key words: *(cosmology:)* dark matter – cosmology: observations – cosmology: theory – galaxies: clusters: general – galaxies: clusters: intracluster medium – galaxies: haloes.

1 INTRODUCTION

Clusters of galaxies are the largest class of gravitationally bound objects to have formed in the universe. The mass content of galaxy clusters is proved to be dominated by elusive dark matter (∼85 per cent), while the vast majority of the baryons residing in the cluster potential well are in the hot X-ray emitting phase (∼10–13 per cent in total mass; e.g. Vikhlinin et al. 2006; Umetsu et al. 2009; Planck Collaboration et al. 2013). Massive galaxy clusters thus contain a wealth of information about the initial conditions for cosmic structure formation and the growth of structure across cosmic time (Frenk et al. 1990; Blandford & Narayan 1992; White, Efstathiou & Frenk 1993; Jenkins et al. 2001; Reiprich & Böhringer 2002).

The distribution of dark matter in quasi-equilibrium haloes, such as galaxy clusters, depends fundamentally on the properties of dark matter. Even though the formation of haloes is a complex and non-linear dynamical process and they are continuously evolving through

accretion and mergers, Lambda cold dark matter (ΛCDM) models predict that the average density profile $\rho(r)$ of collisionless haloes in quasi-gravitational equilibrium is well described by the Navarro–Frenk–White profile (Navarro, Frenk & White 1996, 1997, hereafter NFW) out to their virial radius. The NFW radial density profile is fully specified by two parameters and is defined as

$$\rho(r) = \frac{\delta_c \rho_c}{(r/r_s)(1 + r/r_s)^2}, \tag{1}$$

where ρ_c is the critical density of the universe at the halo redshift z, r_s is the characteristic scale radius at which the logarithmic density slope equals -2, and δ_c sets the normalization of the profile. In this paper, we often describe the NFW model using r_s and the halo mass enclosed within it, $M_s \equiv M(< r_s)$, also referred to as the characteristic scale mass.

According to N-body simulations of ΛCDM models, the structural parameters of the NFW profile, such as halo concentration $c_\Delta \equiv r_\Delta/r_s$, are closely linked to the growth history of individual haloes (Navarro et al. 1997; Ludlow et al. 2013). Here, r_Δ is the overdensity radius at which the mean interior density is Δ times the critical

★ E-mail: ladg84@gmail.com

density of the universe at the specific redshift [i.e. $\Delta \times \rho_c(z)$]. The inner region of haloes ($r \lesssim r_s$) develops in an initial phase of rapid growth, which is often associated to major mergers with other haloes. During the subsequent slow accretion phase, the scale radius r_s stays roughly constant, whereas r_Δ continues to grow through a mixture of physical mass accretion and pseudo-evolution caused by the decrease of ρ_c over time (e.g. Diemer, More & Kravtsov 2013). Haloes thus form 'inside-out'. In this context, haloes that formed earlier tend to present a higher characteristic density $\rho_s \equiv 3M_s/(4\pi r_s^3)$ (Navarro et al. 1997; Zhao et al. 2003; Ludlow et al. 2013). In contrast to $\rho_c(z)$, this characteristic density ρ_s is not constant from cluster to cluster but depends on the formation time of each cluster.

Recently, Fujita et al. (2018a, b) discovered a new Fundamental Plane of galaxy clusters (CFP) using gravitational lensing and X-ray observations of 20 high-mass clusters available from the Cluster Lensing And Supernova survey with *Hubble* (CLASH, Postman et al. 2012; Donahue et al. 2014; Umetsu et al. 2014, 2016; Merten et al. 2015). Fujita et al. (2018b) showed that the 20 CLASH clusters lie on a thin plane defined in the three-dimensional logarithmic space of their characteristic scale radius r_s, mass M_s, and X-ray temperature T_X of the intracluster medium (ICM) with an orthogonal scatter of ~ 0.045 dex. Their findings suggest that the parameters (M_s, r_s) characterizing the internal structure of dark-matter haloes are tightly coupled with the gas temperature T_X. Based on the tight correlation they found, Fujita et al. (2018b) argue that the gas temperature should reflect the potential depth of dark-matter haloes at a specific cluster-formation time, which is encoded in M_s and r_s. Intriguingly, the plane is tilted with respect to $T_X \propto M_s r_s^{-1}$, the plane expected in the case of simplified virial equilibrium. Fujita et al. (2018b) found that this tilt can be explained by a spherical similarity solution for secondary infall and accretion of gas in a matter-dominant universe (Bertschinger 1985), which predicts $T_X \propto M_s^{1.5} r_s^{-2}$ at the cluster scales (Fujita et al. 2018b). They also found that cosmological *N*-body/hydrodynamical simulations reproduce the observed plane and its tilt angle for cluster-scale haloes.

The CFP has been proposed to describe the connection between the thermodynamic history of the intracluster gas and the evolution of the internal structure of dark-matter haloes (Fujita et al. 2018b). With this framework in mind it is clear that studying the CFP as a function of redshift provides an important clue for improving our understanding of how galaxy clusters form and evolve through mergers and accretion. The pioneering works of Fujita et al. (2018a, b), however, did not study in detail to what extent the CFP parameters and scatter depend on the cluster redshift, the dynamical state of clusters, the definition of the gas temperature, and the gas physics and feedback processes implemented in the code. In this paper, we supply this deficiency and present a systematic study of this Fundamental Plane using a sample of ~ 250 simulated cluster-scale haloes (10 times larger than that of Fujita et al. 2018a, b) modelled with full-physics hydrodynamical resimulations by The Three Hundred project (Cui et al. 2018), focusing specifically on the redshift evolution of the plane, the dependence on the dynamical state of haloes, and the stability of the plane against different temperature definitions.

This paper is organized as follows. In Section 2, we present the sample of simulated galaxy clusters of The Three Hundred project as well as the sample of CLASH clusters used in this research. The methodology to determine the parameters defining the CFP is described in Section 3, whereas the CFP obtained from the analysis of The Three Hundred project sample at $z = 0$ is described in Section 4. In Section 5, we study via simulations whether there is an evolution of the CFP with redshift. The dynamical state of The Three Hundred project haloes and its impact on the CFP is explored in Section 6. The

CFP obtained for CLASH clusters by real observations is presented in Section 7. Our results and conclusions are discussed and compared with previous results of the literature in Section 8. Finally, a summary of this research is included in Section 9.

Throughout this paper, we adopt a spatially flat ΛCDM cosmology with the same parameters used in The Three Hundred project based on the Planck 2015 cosmology (Planck Collaboration 2016), namely: Hubble constant of $H_0 = 67.8$ km s^{-1} Mpc^{-1}, $\Omega_M = 0.307$ (total matter density), $\Omega_b = 0.048$ (baryon density), $\Omega_\Lambda = 0.693$ (cosmological constant density), $\sigma_8 = 0.823$ (matter power-spectrum normalization), and $n_s = 0.96$ (scalar spectral index). We use the standard notation M_Δ for the mass enclosed within a sphere of radius r_Δ, within which the mean overdensity equals $\Delta \times \rho_c(z)$ at a particular redshift z. That is, $M_\Delta = (4\pi\Delta/3)\rho_c(z)r_\Delta^3$.

2 GALAXY CLUSTER SAMPLES

2.1 The Three Hundred project

The Three Hundred project (Cui et al. 2018) is composed of 324 galaxy clusters with masses above $M_{200} > 6.24 \times 10^{14}\ h^{-1}\,\mathrm{M}_\odot$ and located at the centre of zoom-in resimulated regions of radius 15 h^{-1} Mpc. These regions were selected from the fiducial *N*-body and dark-matter-only MultiDark Planck 2 simulation at redshift $z = 0$ (MDPL2; Klypin et al. 2016), to subsequently carry out a resimulation with hydrodynamics physics. The MDPL2 has a size of comoving length 1 h^{-1} Gpc and is simulated with 3840^3 dark-matter particles with a mass resolution of $1.5 \times 10^9\ h^{-1}$ Mpc. For the resimulation of The Three Hundred project, the effective mass resolutions for dark matter and gas are $m_{DM} = 1.27 \times 10^9\ h^{-1}\,\mathrm{M}_\odot$ and $m_{gas} = 2.36 \times 10^8\ h^{-1}\,\mathrm{M}_\odot$, respectively. That is, the same combined mass resolution as for MDPL2 according to a baryon fraction of $\Omega_b/\Omega_M \sim 0.16$ (Planck 2015 cosmology).

The Three Hundred project accounts for a broad range of baryonic physics in the GADGET-X code (Rasia et al. 2015), which utilizes a modern Smooth-Particle-Hydrodynamic (SPH) scheme based on a modified version of the GADGET3 code (for details, see Beck et al. 2016). The code implements a supermassive black hole accretion and active galactic nuclei (AGNs) feedback by Steinborn et al. (2015). In addition, the GADGET-X code includes a metal-dependent model for gas cooling (Wiersma, Schaye & Smith 2009), an homogeneous ultraviolet background (following Haardt & Madau 1996), a star-formation model accounting for the metal enrichment of the ICM (Tornatore et al. 2007) assuming a Chabrier (2003) stellar initial mass function, and supernova feedback (Springel & Hernquist 2003). For further details about the GADGET-X code and comparison with respect to other codes and schemes, we refer readers to Cui et al. (2018). It should be noted that although the resimulated Lagrangian regions contain multiple groups and clusters, we focus in this work on the central objects. With the aim of determining the redshift evolution of the CFP, we also study in detail The Three Hundred project clusters at higher redshifts. Specifically, we explore the CFP at $z = 0.00, 0.07, 0.22, 0.33, 0.59,$ and 0.99.

2.2 Galaxy clusters from the CLASH programme

One of the main goals of the CLASH programme was to precisely constrain the mass density profiles of 25 galaxy clusters using deep lensing observations. The sample of galaxy clusters targeted by the CLASH programme is subdivided into two subsamples: (i) 20 hot X-ray clusters with $T_X > 5$ keV and nearly concentric X-ray isophotes, as well as a well-defined X-ray peak closely located to the brightest

cluster galaxy (BCG) position; and (ii) five clusters selected by their exceptional lensing strength (characterized by large Einstein radii, $\theta_{\mathrm{Ein}} > 35$ arcsec, for a fiducial source at redshift $z = 2$) so as to magnify galaxies at high redshift.

It is worth emphasizing that the X-ray subsample was not based on a lensing pre-selection to avoid a biased sample towards intrinsically concentrated clusters and/or those systems where the major axis is preferentially aligned with the line of sight (Hennawi et al. 2007; Oguri & Blandford 2009; Meneghetti et al. 2010). Numerical simulations suggest that the CLASH X-ray-selected subsample is mostly (but not exclusively) composed of relaxed systems ($\sim$70 per cent) and largely free of such orientation bias (Meneghetti et al. 2014, see also Table 1). On the other hand, high-magnification-selected clusters often turn out to be dynamically disturbed as a consequence of highly massive ongoing mergers (Umetsu 2020, see also references therein).

For an observational determination of the Fundamental Plane, we combined redshift and X-ray temperature information detailed in Postman et al. (2012) along with the characteristic scale radius and mass measurements from Umetsu et al. (2016), yielding a subsample of 20 CLASH clusters composed of 16 X-ray-selected and four high-magnification clusters (see Section 3.4 for further details). It should be noted that five of the 25 clusters of the CLASH sample were not included in the joint lensing analysis performed by Umetsu et al. (2016) because they lacked of usable wide-field ground-based weak-lensing data (see Umetsu et al. 2014). Consequently, they were also excluded in this work. The CLASH subsample spans a redshift range of $0.19 \leq z \leq 0.69$ with a median redshift of 0.35. Umetsu et al. (2016) found that the stacked strong- and weak-lensing signal of the CLASH X-ray-selected subsample is best described by the NFW model. In Table 1, we summarise the main properties of the CLASH clusters used in this work. As a consequence of the CLASH selection, all the clusters show X-ray temperatures higher than 5 keV.

In Fig. 1, we show the distributions of M_{200}, r_{200}, c_{200}, and T_X (obtained in the radial range 50–500 h^{-1} kpc, further details in Section 3.4) for both observed and simulated clusters studied in this work. As a consequence of the CLASH pre-selection of $T_X > 5$ keV, we see that The Three Hundred project includes clusters with spectroscopic-like temperatures much lower than the CLASH sample (see the left-hand and middle panels in Fig. 1). On the other hand, the radius and mass distributions of The Three Hundred project sample at $T_{\mathrm{sl}} > 5$ keV properly match the ranging values of the CLASH sample. In terms of concentration, the values for the simulated $T_{\mathrm{sl}} > 5$ keV clusters span the range from $\sim$2 to $\sim$9, while all the CLASH clusters present concentrations of $c_{200} \lesssim 8$ within the 1σ uncertainty level. The Three Hundred project sample thus includes clusters with slightly higher concentrations than estimated for the 20 CLASH clusters. We refer to Merten et al. (2015) and Umetsu et al. (2016) for detailed studies of the CLASH concentration–mass relation and Meneghetti et al. (2014) for its theoretical prediction. Although the CLASH sample is composed of X-ray and lensing-selected clusters, in contrast to the mass-selected The Three Hundred project sample, we find a proper overlap of both samples in the parameter space (see Fig. 1).

Finally, it is not possible to verify whether the two samples have similar relaxation states and formation times, because the dynamical states of individual CLASH clusters are uncertain. Nevertheless, the fraction of relaxed clusters in The Three Hundred project sample (typically below 40 per cent; see Cui et al. 2018) is lower than predicted for the CLASH sample ($\sim$70 per cent). In this context, the CLASH sample may not be faithfully representative of the full cluster population with $T_X > 5$ keV.

3 CONSTRAINTS ON THE CFP: METHODOLOGY

A detailed dissection of the CFP involves a set of cluster parameters that need to be constrained in a reliable manner. For simulated clusters, the characteristic scale parameters can be directly obtained from an NFW fit to the three-dimensional mass distribution (see Section 3.1), and we can compute the global gas temperature of the ICM by choosing an appropriate weighting scheme (see Section 3.2). Moreover, we can explore the influence of the dynamical relaxation state of each individual cluster on the definition of the CFP (see Section 3.3). For CLASH clusters, we employ measurements of the characteristic scale parameters and the X-ray gas temperature from the published literature (see Section 3.4), which are subject to observational uncertainties and systematics. Finally, various methods to determine the CFP are considered and the minimum distance method (MINDISQ) has been selected as the most reliable one (Section 3.5).

3.1 NFW fitting of simulated clusters

From The Three Hundred project hydrodynamical simulations, we extract the total mass profiles $M(< r)$ of individual clusters considering all particle species (dark matter, gas, and stars) in three-dimensional spherical shells. Subsequently, we fit the three-dimensional mass profiles with a corresponding parametric NFW mass description. For the minimization procedure, we use the Levenberg–Marquardt algorithm implemented in the MPFITFUN[1] routine of IDL.[2] The fitting procedure, in addition to the normalization, returns the scale radius, which we use to compute the characteristic mass, M_{s}.

For the fitting procedure of The Three Hundred project clusters at $z = 0$, we fit the NFW formula to the mass profiles with the radial range $[0.08, 1.0] \times r_{100}$. For the cluster simulations at higher redshifts ($z = 0.07, 0.22, 0.33, 0.59$, and 0.99), the NFW fit was performed in the radial range $[0.1, 1.0] \times r_{200}$. The innermost parts of clusters, or cores, were excised during the determination of the characteristic parameters to not be affected by the numerical resolution of our sample. This excision is common in literature since the interactions in the inner bins are dominated by two-body collisions (Mostoghiu et al. 2019) and the density profile at $r < 7$ h^{-1} kpc can deviate from an NFW profile becoming steeper for the presence of the BCG, which may dominate the mass profile with respect to a dark-matter-only NFW profile (Schaller et al. 2015).

We exclude from the following analysis all clusters non properly described by an NFW profile, meaning that we use only objects with $\sigma_{\mathrm{fit}} \equiv \chi^2/\mathrm{dof} \leq 2$ (average sum of the squared residuals per degree of freedom) and we exclude the systems whose scale radius is equal to the lower and upper bounds imposed during the minimization process (0.01 and 1.0 h^{-1} Mpc). These two criteria were applied for all NFW profiles at any redshift to facilitate the interpretation and understanding of this fundamental relation (details in Section 5). The number of clusters in our sample at $z = 0$ amounts to $\sim$245, whereas at higher redshift this value ranges from 231 to 280 clusters (more details in Section 5).

Table 1. Properties of galaxy clusters selected from CLASH. All halo mass and radius measurements were obtained from a joint strong lensing, weak lensing shear-and-magnification analysis of Umetsu et al. (2016), whereas the rest of properties were taken from Postman et al. (2012).

Cluster	RA (deg)	DEC (deg)	z	M_{200} ($10^{14}\,h^{-1}\,M_\odot$)	r_{200} (h^{-1} kpc)	M_s ($10^{14}\,h^{-1}\,M_\odot$)	r_s (h^{-1} kpc)	T_X (keV)
X-ray-selected								
Abell 383	42.014	− 3.529	0.187	$5.51^{+2.16}_{-1.56}$	1261^{+147}_{-132}	$0.99^{+0.70}_{-0.39}$	215^{+111}_{-69}	6.5 ± 0.24
Abell 209[a]	22.969	− 13.611	0.206	$10.76^{+2.49}_{-2.26}$	1567^{+112}_{-118}	$3.64^{+1.50}_{-1.12}$	584^{+167}_{-133}	7.3 ± 0.54
Abell 2261[a]	260.614	+32.133	0.224	$16.11^{+3.88}_{-3.31}$	1782^{+133}_{-132}	$4.10^{+1.91}_{-1.30}$	480^{+163}_{-120}	7.6 ± 0.30
RX J2129.7+0005	322.416	+ 0.089	0.234	$4.25^{+1.40}_{-1.08}$	1139^{+113}_{-108}	$0.80^{+0.48}_{-0.29}$	205^{+93}_{-61}	5.8 ± 0.40
Abell 611	120.237	+36.057	0.288	$10.96^{+3.36}_{-2.85}$	1534^{+143}_{-146}	$2.69^{+1.63}_{-1.04}$	395^{+174}_{-123}	7.9 ± 0.35
MS 2137−2353	325.063	− 23.661	0.313	$9.36^{+4.08}_{-3.32}$	1443^{+185}_{-196}	$3.22^{+3.62}_{-1.79}$	543^{+392}_{-244}	5.9 ± 0.30
RX J2248.7−4431[a]	342.185	− 44.530	0.348	$12.93^{+5.40}_{-3.97}$	1587^{+196}_{-183}	$3.43^{+3.28}_{-1.60}$	449^{+292}_{-170}	12.4 ± 0.60
MACS J1115.9+0129	168.967	+ 1.499	0.352	$11.64^{+2.79}_{-2.53}$	1530^{+114}_{-120}	$3.61^{+1.71}_{-1.20}$	518^{+179}_{-135}	8.0 ± 0.40
MACS J1931.8−2635	292.957	− 26.576	0.352	$10.39^{+6.21}_{-3.89}$	1473^{+249}_{-213}	$2.38^{+3.16}_{-1.26}$	347^{+300}_{-152}	6.7 ± 0.40
RX J1532.9+3021	233.224	+30.350	0.363	$4.17^{+1.74}_{-1.48}$	1083^{+134}_{-147}	$0.85^{+1.13}_{-0.35}$	207^{+304}_{-80}	5.5 ± 0.40
MACS J1720.3+3536	260.071	+35.607	0.391	$10.09^{+3.28}_{-2.69}$	1439^{+142}_{-141}	$2.39^{+1.58}_{-0.94}$	354^{+171}_{-112}	6.6 ± 0.40
MACS J0429.6−0253	67.400	− 2.886	0.399	$6.72^{+2.84}_{-2.06}$	1253^{+156}_{-144}	$1.45^{+1.24}_{-0.64}$	274^{+164}_{-99}	6.0 ± 0.44
MACS J1206.2−0847[a]	181.551	− 8.801	0.440	$12.68^{+3.07}_{-2.77}$	1526^{+114}_{-120}	$3.24^{+1.69}_{-1.12}$	412^{+169}_{-121}	10.8 ± 0.60
MACS J0329.7−0211[a]	52.424	− 2.197	0.450	$6.02^{+1.49}_{-1.24}$	1186^{+91}_{-88}	$1.00^{+0.43}_{-0.28}$	177^{+65}_{-44}	8.0 ± 0.50
RX J1347.5−1145[a]	206.877	− 11.753	0.451	$23.85^{+6.60}_{-5.57}$	1876^{+159}_{-159}	$6.90^{+3.91}_{-2.50}$	588^{+236}_{-167}	15.5 ± 0.60
MACS J0744.9+3927[a]	116.220	+39.457	0.686	$12.53^{+3.72}_{-3.16}$	1386^{+126}_{-128}	$3.40^{+2.17}_{-1.36}$	401^{+190}_{-133}	8.9 ± 0.80
High-magnification-selected								
MACS J0416.1−2403	64.039	− 24.068	0.396	$7.49^{+1.90}_{-1.69}$	1301^{+102}_{-106}	$2.37^{+1.07}_{-0.77}$	450^{+143}_{-109}	7.5 ± 0.80
MACS J1149.5+2223	177.399	+22.399	0.544	$17.43^{+4.06}_{-3.63}$	1632^{+118}_{-122}	$7.50^{+3.74}_{-2.55}$	776^{+281}_{-202}	8.7 ± 0.90
MACS J0717.5+3745	109.382	+37.755	0.548	$18.68^{+3.89}_{-3.54}$	1668^{+108}_{-113}	$9.19^{+3.65}_{-2.67}$	907^{+240}_{-188}	12.5 ± 0.70
MACS J0647.7+7015	101.958	+70.247	0.584	$9.66^{+3.20}_{-2.67}$	1321^{+132}_{-135}	$2.32^{+1.64}_{-0.96}$	329^{+178}_{-114}	13.3 ± 1.80

Notes.

[a]Clusters with any substructure according to reports based on X-ray morphology (Schmidt & Allen 2007; Maughan et al. 2008; Postman et al. 2012).
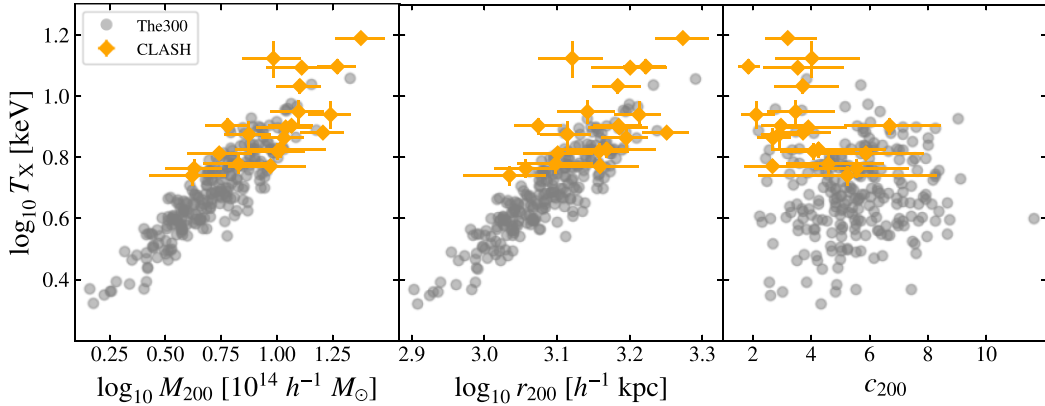

Figure 1. Mass, radius, and concentration (horizontal axis, from left to right) versus X-ray temperature (vertical axis, T_X extracted in the radial range 50–500 h^{-1} kpc) of the CLASH cluster sample (at a median redshift of $z = 0.36$; orange diamonds) and simulated galaxy clusters of The Three Hundred project (at $z = 0.33$; grey circles) for spectroscopic-like temperatures (vertical axis, T_{sl} measured within the range 50–500 h^{-1} kpc). Vertical and horizontal bars show the 1σ errors of parameters for CLASH clusters.

3.2 Temperature measurements of simulated clusters

As a result of the two-phase accretion, typical of galaxy clusters, the formation time and evolution of these massive haloes is encoded in the thermodynamic history of the diffuse hot gas residing in the cluster potential well. Indeed, the largest variation in gas temperature happens as a consequence of major mergers and somehow reflects the assembly of the internal structure of cluster-scale haloes.

We compute gas temperatures for a set of radial ranges to explore the impact of this choice on the resulting parameters defining the Fundamental Plane, as well as their implications. In this work, we compute average temperatures in radial ranges of $[0.1, 1.0] \times r_{200}$, $[0.15, 1.0] \times r_{500}$, and $[50, 500] \times h^{-1}$ kpc. These gas temperatures are denoted as $T(r_{200})$, $T(r_{500})$, and $T(500\,h^{-1}$ kpc$)$, respectively.

In addition, two definitions of weighted temperatures were used: mass-weighted and spectroscopic-like temperatures. For the former,

the weighting function is the associated mass for each gas element in the ICM (see e.g. Kang et al. 1994; Bartelmann & Steinmetz 1996; Mathiesen & Evrard 2001) and it is more physically motivated. On the other hand, the spectroscopic-like temperature better approximates spectroscopic temperatures from X-ray observations (Mazzotta et al. 2004). Formally, these temperatures are respectively expressed as follows:

$$T_{mw} = \frac{\int m \, T \, dV}{\int m \, dV} = \sum_i m_i \, T_i / \sum_i m_i ,\qquad (2)$$

$$T_{sl} = \frac{\int n^2 T^{1/4} \, dV}{\int n^2 T^{-3/4} \, dV} = \sum_i n_i^2 T_i^{1/4} / \sum_i n_i^2 T_i^{-3/4} ,\qquad (3)$$

where m_i is the mass of the ith gas element, n_i is the gas density, and T_i is its temperature. We note that spectroscopic-like temperatures serve as a useful proxy for X-ray temperatures obtained from real observations (Mazzotta et al. 2004), which also facilitates any interpretation of observational results against simulations.

3.3 Dynamical state parameters of simulated clusters

Within the simulated Lagrangian regions, haloes and subhaloes were identified with the AHF code (Knollmann & Knebe 2009). These catalogues were used to compute different indicators for the cluster dynamical relaxation. The first indicator, derived from the merger tree of each halo, is the formation redshift, z_{form}, defined in Mostoghiu et al. (2019) as the redshift at which half of the mass M_{200} at present was already accreted, meaning that

$$z_{form} = -\ln(0.5)/\lambda ,\qquad (4)$$

where λ is the mass accretion rate of the halo and the accretion history of each cluster is assumed as the functional form proposed by Wechsler et al. (2002) or equivalently

$$M_{200}(z_{form}) = M_{200}^{z=0} \exp(-\lambda z) .\qquad (5)$$

The other dynamical relaxation indicators are the virial ratio (η), the centre-of-mass offset (Δ_r), and the fraction of mass in subhaloes (f_s; see Cui et al. 2018). In brief, η relies on the kinetic, potential energy and surface pressure to determine the dynamical state of a cluster (Cui et al. 2017), Δ_r on the deviation of the centre of mass with respect to the maximum density peak of the halo, and f_s on the fraction of mass in subhaloes. These three indicators were measured within the radius r_{200}. In addition, we considered an extra indicator that combines the three indicators just mentioned (see also Haggar et al. 2020; De Luca et al. 2021, and further details in Section 6) formally expressed as

$$\chi_{DS} = \left[\frac{\left(\frac{|1-\eta|}{0.15}\right)^2 + \left(\frac{\Delta_r}{0.04}\right)^2 + \left(\frac{f_s}{0.1}\right)^2}{3} \right]^{-\frac{1}{2}} .\qquad (6)$$

3.4 Fundamental Plane parameters of the CLASH sample

Using high-quality gravitational-lensing data available for the CLASH sample, Umetsu et al. (2016) reconstructed binned surface mass density profiles for 16 X-ray-selected and four high-magnification CLASH clusters. Their lensing analysis combines wide-field shear and magnification weak-lensing constraints primarily from the *Subaru* telescope (Umetsu et al. 2014) and small-scale weak and strong lensing constraints from the *Hubble Space Telescope* (Zitrin et al. 2015). All individual mass profiles were subsequently fitted to a projected NFW profile within 2 h^{-1} Mpc using the full covariance matrix (see Umetsu et al. 2016; Umetsu 2020). The

NFW characteristic parameters r_s and M_s were determined from the posterior distributions of the NFW parameters M_{200} and c_{200} (for further details, see Umetsu et al. 2016). It should be noted that the r_s and M_s parameters for The Three Hundred project are obtained from a three-dimensional analysis, whereas the NFW parameters for the CLASH clusters were derived from the projected lensing profiles assuming a spherical NFW halo. The effect of scatter due to triaxial halo shapes was properly accounted for in the covariance matrix for each individual cluster (Umetsu et al. 2016). On the other hand, as discussed earlier (see Section 2.2), the CLASH sample should not be affected by orientation bias, so that the NFW parameters estimated for the CLASH sample are not expected to be significantly affected by the projection effects.

All CLASH clusters have observations from the *Chandra X-ray Observatory* and derived X-ray properties (Postman et al. 2012; Donahue et al. 2014). In particular, the X-ray temperatures presented in Postman et al. (2012) were obtained using core-excised *Chandra* spectra within a uniform radial range extending from 50 h^{-1} to 500 h^{-1} kpc. The X-ray temperatures obtained in this way are unaffected by the presence of a cool core (see e.g. Markevitch 1998). For the cosmological parameters used in The Three Hundred project, this radial range corresponds to 73.75 and 737.5 kpc, respectively.

3.5 Determination of the Fundamental Plane of clusters

The CFP is expressed by an equation of the form $T \propto M_s^\alpha r_s^\beta$, where the coefficients α and β are tightly connected to the properties of the dark-halo structure. Therefore, α and β are the most relevant parameters in this work. In fact, their values can be predicted for different theoretical scenarios and/or under certain assumptions about the relaxation/thermalization processes. For instance, in case of simplified virial equilibrium, we expect values of $\alpha = 1$ and $\beta = -1$, while the similarity solution for a secondary infall model (Bertschinger 1985; Fujita et al. 2018a, b) implies $\alpha = 1.5$ and $\beta = -2$. To facilitate our analysis and interpretation, we characterize the CFP in the following form:

$$\log_{10}\left(\frac{T}{T_0}\right) = \alpha \, \log_{10}\left(\frac{M_s}{M_{s,0}}\right) + \beta \, \log_{10}\left(\frac{r_s}{r_{s,0}}\right) + \delta ,\qquad (7)$$

where $M_{s,0}$, $r_{s,0}$, and T_0 are respectively the median values of the characteristic scale mass, radius, and temperature (mass-weighted, spectroscopic-like, or X-ray temperature) of the clusters employed to fit the CFP. As a reference, these median values correspond to $M_{s,0} = 2.03 \times 10^{14} \, h^{-1} \, M_\odot$, $r_{s,0} = 424 \, h^{-1}$ kpc, and $T_0 = 5.0$–6.7 keV (depending on the temperature definition and radial range) for The Three Hundred project clusters (see also Section 4); whereas for the CLASH clusters these are $M_{s,0} = 2.98 \times 10^{14} \, h^{-1} \, M_\odot$, $r_{s,0} = 407 \, h^{-1}$ kpc, and $T_{X,0} = 7.8$ keV (see also Section 7). In equation (7), there is another parameter denoted as δ, which is the normalization of the CFP. When $\delta = 0$, the plane is centred at the sample median values ($M_{s,0}$, $r_{s,0}$, and T_0). We note that both α and β are not affected by the choices of T_0, $M_{s,0}$, and $r_{s,0}$, only the normalization δ shifts accordingly.

One of the goals of this work is to determine the α and β parameters that characterize the CFP (equation 7) in the most reliable way. To this end, we have explored several methods to perform fitting of the CFP, such as the χ^2-minimization method, the principal component analysis (PCA), the two-dimensional least-squares minimization, and the MINDISQ. The main difference among them is the choice of the parameter or reference quantity used to minimize and find the best-fitting plane. We examined in detail the results obtained from the four fitting methods to conclude that the most reliable method

Table 2. Best-fitting parameters (α, β, and δ) and thickness (σ_d in dex units) of the Fundamental Plane defined in the ($\log_{10} r_s$, $\log_{10} M_s$, and $\log_{10} T$) space obtained for a sample of 245 simulated galaxy clusters at $z = 0$ (see equation 7) from The Three Hundred project with $\sigma_{fit} \leq 2$. The results are shown separately for the mass-weighted and spectroscopic-like temperatures (T_{mw} and T_{sl}, respectively) computed within a radial range of 500 h^{-1} kpc, r_{500}, and r_{200} (see further details in the text). All results were obtained by setting $M_{s,0} = 2.03 \times 10^{14}\ h^{-1}\ M_\odot$ and $r_{s,0} = 424\ h^{-1}$ kpc. For each quantity, the lower and upper errors enclose the 1σ uncertainty range.

	α	β	δ	σ_d (dex)	T_0 (keV)
$T_{mw}(500\ h^{-1}$ kpc$)$	$1.10^{+0.04}_{-0.03}$	$-1.22^{+0.05}_{-0.05}$	$0.001^{+0.003}_{-0.003}$	0.021	6.66
$T_{mw}(r_{500})$	$0.99^{+0.02}_{-0.02}$	$-1.09^{+0.03}_{-0.03}$	$-0.001^{+0.002}_{-0.002}$	0.015	5.62
$T_{mw}(r_{200})$	$0.96^{+0.02}_{-0.02}$	$-1.02^{+0.03}_{-0.03}$	$-0.001^{+0.002}_{-0.002}$	0.015	5.05
$T_{sl}(500\ h^{-1}$ kpc$)$	$1.22^{+0.06}_{-0.05}$	$-1.50^{+0.08}_{-0.09}$	$-0.007^{+0.004}_{-0.004}$	0.030	6.26
$T_{sl}(r_{500})$	$1.10^{+0.04}_{-0.03}$	$-1.36^{+0.05}_{-0.05}$	$-0.003^{+0.003}_{-0.003}$	0.018	5.54
$T_{sl}(r_{200})$	$1.12^{+0.04}_{-0.03}$	$-1.43^{+0.04}_{-0.05}$	$-0.006^{+0.003}_{-0.003}$	0.020	5.32
$T_{sl}(500\ h^{-1}$ kpc$) > 5$ keV	$1.27^{+0.07}_{-0.06}$	$-1.45^{+0.07}_{-0.08}$	$-0.012^{+0.004}_{-0.004}$	0.026	6.63
Number = 245		$M_{s,0} = 2.03 \times 10^{14}\ h^{-1}\ M_\odot$		$r_{s,0} = 424\ h^{-1}$ kpc	

for this study is the MINDISQ method. For this method, the CFP corresponds to the plane that minimizes the total sum of squared distances to the distribution of points, $\delta s^2 := \sum_i d_i^2$, where $|d_i|$ is the distance of each cluster to the CFP and d_i is expressed as

$$d_i = \frac{\alpha \log_{10} M_{i,s} + \beta \log_{10} r_{i,s} - \log_{10} T_i + \delta}{\sqrt{\alpha^2 + \beta^2 + 1}}.\qquad(8)$$

By construction, this method provides the lowest dispersion or thickness (σ_d) of the distribution of points around the resulting plane, which we define as half of the difference between the 84th and 16th percentiles of the distribution of d_i values (distances to the best-fitting CFP). We note that points above (below) the CFP yield positive (negative) d_i values.

Using the MINDISQ method, we compute the CFP of the simulated clusters from The Three Hundred project (Section 4), as well as of the real clusters from CLASH (Section 7) to compare these results. It is worth mentioning that the α and β values obtained via the MINDISQ method are found to be quite similar to the results using PCA techniques. The main difference between the two methods is that PCA assumes that the plane is centred on the point ($M_{s,0}$, $r_{s,0}$, T_0), which acts as a pivot point. This is not the case for the MINDISQ method because of the additional degree of freedom, δ, which in turn avoids the possibility that α and β are affected by the particular choice of T_0, $M_{s,0}$, and $r_{s,0}$. For this reason and to be consistent with the CFP coefficients obtained for The Three Hundred project clusters, our CFP analysis of the CLASH sample is performed using the MINDISQ method in this work.

In addition, we explored the uncertainties of the CFP parameters, as well as their correlations. For The Three Hundred project sample, we performed a bootstrapping analysis. In particular, we built 10^4 bootstrap samples composed of 245 clusters by using sampling with replacement from the simulated clusters with $\sigma_{fit} \leq 2$. For each of the bootstrap samples, we obtained a set of α, β, and δ values by the MINDISQ method. The uncertainties and correlations of the parameters are obtained by the three sets of 10^4 values. On the other hand, to estimate the uncertainties on the CFP parameters for the CLASH sample, we used the marginalized posterior distributions of M_s and r_s obtained by Umetsu et al. (2016; 10^4 steps) and assumed uncorrelated Gaussian errors for the X-ray temperature obtained from *Chandra* (Postman et al. 2012).

4 FUNDAMENTAL PLANE IN THE THREE HUNDRED PROJECT AT $z = 0$

We selected clusters at $z = 0$ from The Three Hundred project according to the goodness of fit of the NFW model, $\sigma_{fit} \leq 2$, resulting in a sample composed of 245 clusters. The sample spans characteristic halo masses of $M_s \in [0.14, 7.05] \times 10^{14}\ h^{-1}\ M_\odot$ and characteristic scale radii of $r_s \in [149, 1003] \times\ h^{-1}$ kpc, whose median values are $M_{s,0} = 2.03 \times 10^{14}\ h^{-1}\ M_\odot$ and $r_{s,0} = 424\ h^{-1}$ kpc, respectively. Depending on the definition of the weighted temperature, as well as the region in which this temperature is computed, the gas temperatures of the sample vary within the range $T \in [1.1, 15.2]$ keV (the minimum value refers to the spectroscopic-like temperature within r_{200} and the maximum to the mass-weighted temperature within $r < 500\ h^{-1}$ kpc). In this sense, the median gas temperature ranges from 5.0 to 6.7 keV and gas temperatures in inner regions ($r < 500\ h^{-1}$ kpc) exhibit higher values than those within r_{500} and r_{200} (the temperature median values in Table 2).

In Table 2, we illustrate the results for all gas temperature definitions for The Three Hundred project obtained with the MINDISQ method. The first conclusion from the MINDISQ analysis (also obtained for the other methods explored in this work) is that the clusters from The Three Hundred project lie on a thin plane, as shown in Fig. 2. Secondly, the dispersion or thickness of this plane depends on the gas temperature definition and it spans a range of values of $\sigma_d \in [0.015, 0.030]$ dex (average thickness of 0.02 dex; see Fig. 2 and Table 2). The thickness is systematically lower for the mass-weighted gas temperature than for the spectroscopic-like one. Thirdly, the values of α, β, and δ that define the CFP (see equation 7) also vary according to the gas temperature definition employed.

Regarding the best-fitting values of α and β, it should be noted that for all temperature definitions in The Three Hundred project, we find $1 < \alpha < 1.5$ and $-2 < \beta < -1$, that is, halfway between the expectation for simplified virial equilibrium and the similarity solution for a secondary infall model. In fact, the case for the mass-weighted temperature within r_{200} [$T_{mw}(r_{200})$, see Table 2] is fully compatible with the simplified virial expectation within a 1σ uncertainty level. In general, we find that The Three Hundred project results for the mass-weighted temperature are closer to the virial expectation, while the results for the spectroscopic-like temperature show intermediate values between the virial expectation and the similarity solution.
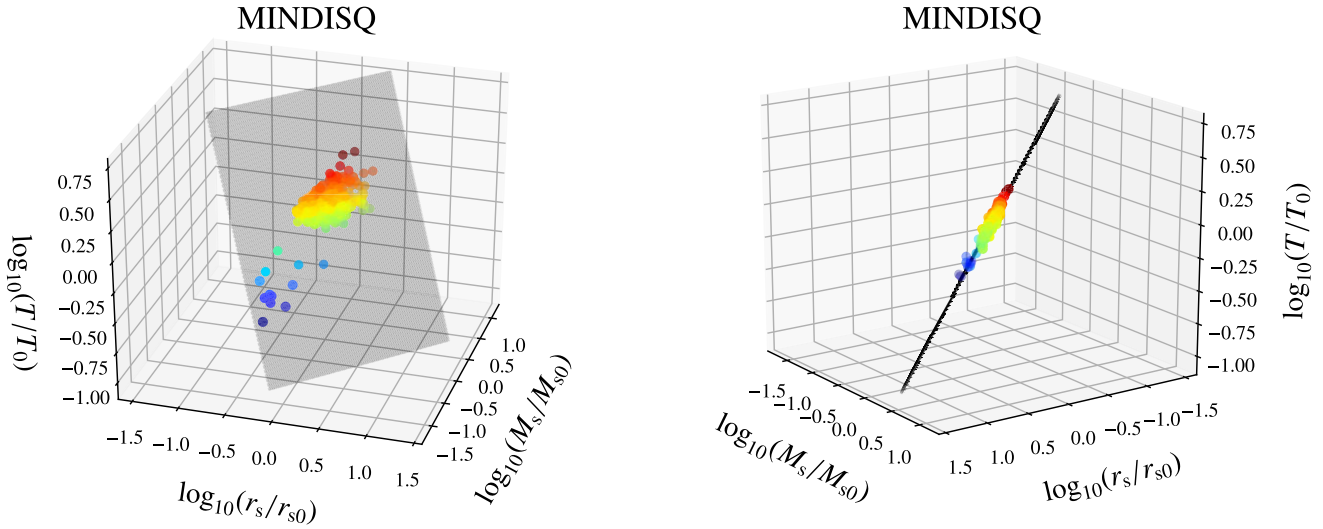
Figure 2. Distribution of 245 simulated galaxy clusters at $z = 0$ from The Three Hundred project with $\sigma_{\rm fit} \leq 2$ across the Fundamental Plane defined in the ($\log_{10}M_{\rm s}$, $\log_{10}r_{\rm s}$, and $\log_{10}T$) space where $M_{\rm s,0} = 2.03 \times 10^{14}\ h^{-1}\ {\rm M}_\odot$, $r_{\rm s,0} = 424\ h^{-1}$ kpc, and $T_0 = 5.05$ keV. All clusters are colour-coded according to their mass-weighted temperatures ($\log_{10}T/T_0$) measured in the radial range [0.1, 1.0] × r_{200}. Left-hand panel: Best-fitting plane (grey) obtained with the MINDISQ method (further details in the text). Right-hand panel: Same as left-hand panel, but from a different viewing angle to illustrate the low dispersion of the clusters with respect to the best-fitting plane.

There is evidence of systematic trends between (α, β) and the temperature definition used to define the CFP (Table 2). First, the α and β values are similar in the cases of $T(r_{500})$ and $T(r_{200})$, in which the temperatures were measured within apertures that are much larger than the halo scale radius, $r_{\rm s}$. For $T(500\ h^{-1}$ kpc) where gas temperatures were measured within a fixed aperture that is close to the median value of $r_{\rm s}$, the resulting CFP deviates the most from the virial expectation and shifts towards the similarity solution. Second, the CFPs obtained with $T_{\rm sl}$ exhibit systematically higher (lower) values of α (β) compared to those obtained with $T_{\rm mw}$ computed within the same radial range. As a result, the CFPs with $T_{\rm sl}$ tend to be more shifted towards the similarity solution than those with $T_{\rm mw}$. Since the spectroscopic-like temperature is more sensitive to the inner ICM region than the mass-weighted one, both trends indicate that the systematic deviations from the virial expectation are likely caused by the inner temperature distribution ($r \lesssim r_{\rm s}$). We note that α and β are anticorrelated, whereas δ appears to be uncorrelated with respect to the other two parameters (Fig. 3).

We also derive a CFP for clusters with spectroscopic-like temperatures of $T_{\rm sl}(500\ h^{-1}$ kpc) > 5 keV, mimicking the CLASH X-ray selection (see Table 2 and Fig. 1). There are 201 clusters in The Three Hundred project with $T_{\rm sl}(500\ h^{-1}$ kpc) > 5 keV and $\sigma_{\rm fit} \leq 2$. We find that the α and β values mildly change with respect to the ones obtained for the full sample in the same region, reaching a similar conclusion.

5 THE FUNDAMENTAL PLANE OF CLUSTERS AT DIFFERENT REDSHIFT

The redshift evolution of the CFP is explored using clusters from The Three Hundred project. For this aim, we use our set of characteristic parameters and gas temperatures for the simulated clusters at higher redshifts in the simulation ($z = 0.07, 0.22, 0.33, 0.59,$ and 0.99). As in previous sections, the CFP at each redshift is determined using the MINDISQ method and only using those clusters that were properly fitted by an NFW profile (i.e. $\sigma_{\rm fit} \leq 2$). As a result, the number of
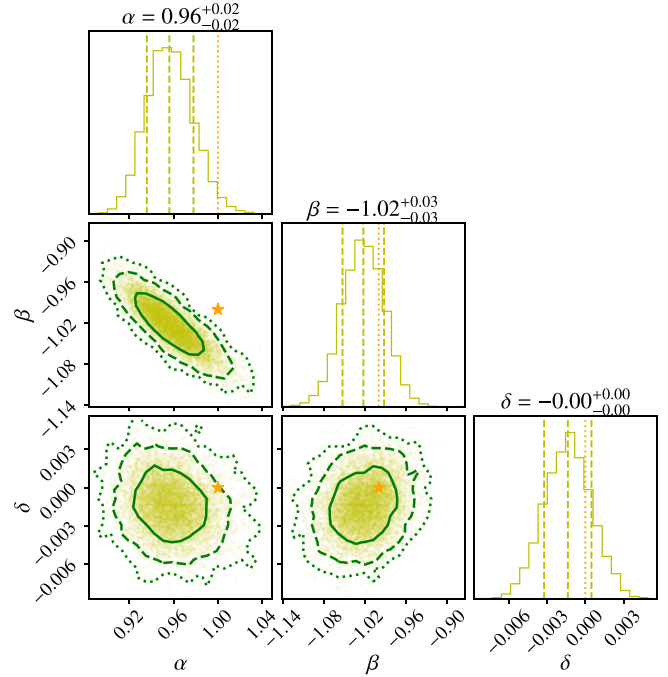

Figure 3. Constraints on the parameters (α, β, and δ) defining the Fundamental Plane (see equation 7) of galaxy clusters at $z = 0$ from The Three Hundred project obtained using mass-weighted temperatures within r_{200}. Green solid, dashed, and dotted lines illustrate the confidence levels of 68, 95, and 99.7 per cent of probability, respectively. Dashed yellow lines denote the 16th, 50th, and 84th percentiles of the distributions of parameters obtained from bootstrapping. In each panel, the orange star-shaped symbol or the vertical dotted line indicates the expectation for the simplified virial equilibrium case.

Table 3. Redshift-dependent coefficients of the Fundamental Plane, $\alpha(z) = \alpha_0 (1 + z)^{\alpha_1}$ and $\beta(z) = \beta_0 (1 + z)^{\beta_1}$, for The Three Hundred project galaxy clusters.

	α_1	α_0	β_1	β_0
$T_{\mathrm{mw}}(500\,h^{-1}\,\mathrm{kpc})$	$-0.11^{+0.04}_{-0.04}$	$1.15^{+0.02}_{-0.02}$	$-0.14^{+0.06}_{-0.05}$	$-1.30^{+0.03}_{-0.03}$
$T_{\mathrm{mw}}(r_{500})$	$-0.17^{+0.04}_{-0.04}$	$1.05^{+0.02}_{-0.02}$	$-0.19^{+0.05}_{-0.05}$	$-1.19^{+0.03}_{-0.03}$
$T_{\mathrm{mw}}(r_{200})$	$-0.13^{+0.04}_{-0.04}$	$1.01^{+0.02}_{-0.02}$	$-0.16^{+0.06}_{-0.06}$	$-1.12^{+0.03}_{-0.03}$
$T_{\mathrm{sl}}(500\,h^{-1}\,\mathrm{kpc})$	$-0.26^{+0.05}_{-0.06}$	$1.22^{+0.03}_{-0.03}$	$-0.24^{+0.07}_{-0.07}$	$-1.47^{+0.04}_{-0.05}$
$T_{\mathrm{sl}}(r_{500})$	$-0.34^{+0.05}_{-0.05}$	$1.19^{+0.03}_{-0.03}$	$-0.39^{+0.06}_{-0.07}$	$-1.50^{+0.04}_{-0.04}$
$T_{\mathrm{sl}}(r_{200})$	$-0.35^{+0.05}_{-0.05}$	$1.23^{+0.03}_{-0.02}$	$-0.40^{+0.06}_{-0.06}$	$-1.56^{+0.04}_{-0.04}$

clusters used to determine the CFP at each redshift can vary: at $z = 0.99$, there are 280 clusters, then the number of objects decreases down to 231 for $z = 0.07$. For each redshift, the uncertainties and correlations of the α, β, and δ parameters were determined using 10^4 bootstrap samples.

As summarized in Table A1 (see Appendix A), the best-fitting α and β parameters defining the CFP span the ranges of $0.9 < \alpha < 1.3$ and $-1.6 < \beta < -1$ at $z < 1$. As found for the CFP at $z = 0$ (Section 4), the best-fitting values of α and β depend on the gas temperature definition (mass-weighted and spectroscopic-like) and on their radial ranges (see Table A1 in Appendix A). The absolute values of α and β are slightly larger for the spectroscopic-like temperature with respect to the mass-weighted one. This is especially true for the outer regions (r_{500} and r_{200}) compared to that obtained for the radial range of $500\,h^{-1}$ kpc. We notice that for the mass-weighted temperature inside r_{200}, $T_{\mathrm{mw}}(r_{200})$, the CFP is very close to the virial expectation ($\alpha = 1$ and $\beta = -1$). However, we stress again that $T_{\mathrm{mw}}(r_{200})$ is measured within an aperture that is much larger than the halo scale radius r_{s} (see the distribution of $c_{200} = r_{200}/r_{\mathrm{s}}$ in the right-hand panel of Fig. 1).

Regarding the CFP thickness, we find that there are subtle differences between the mass-weighted and the spectroscopic-like temperatures, where σ_{d} tends to be marginally higher (of the order of ~ 10 per cent) for the latter.

To quantify the evolution of the CFP with redshift, we assume that α and β are redshift-dependent parameters. Specifically, we parametrize the redshift evolution of the CFP parameters as follows: $\alpha(z) = \alpha_0 (1 + z)^{\alpha_1}$ and $\beta(z) = \beta_0 (1 + z)^{\beta_1}$. As a consequence, $\alpha_1 = \beta_1 = 0$ implies no evolution of the CFP. To determine the uncertainties of the parameters, we performed this fit on the bootstrap samples, obtaining 10^4 sets of (α_0, α_1, β_0, β_1) values for each of the temperatures and radial ranges (see Table 3).

According to The Three Hundred project simulations, there are hints for an evolution of α and β since $z \sim 1$ (see Table 3 and Fig. 4). Specifically, our results point out that the CFP may gradually change with redshift and this trend is consistent for all temperature definitions and radial ranges probed. Using the mass-weighted temperature, the evolution of the two parameters, α and β, is mild with a maximum of 15 per cent between $z = 1$ and $z = 0$, while in the same temporal range they vary with a maximum of 25 per cent for the spectroscopic-like temperature. It is noteworthy that based on The Three Hundred project simulations, we would expect that clusters form a CFP similar to the virial expectation at $z = 1$, which evolves into a CFP that is halfway between the virial expectation and the similarity solution for a secondary infall model. In general, all cases exhibit α and β closer to the virial expectation ($\alpha = 1$ and $\beta = -1$) at higher redshifts. Notice that at all times, the scatter around the CFP remains very low
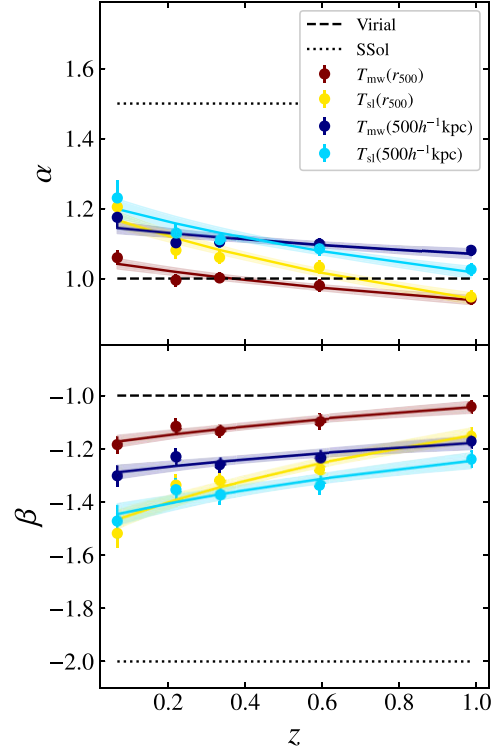

Figure 4. Evolution of the parameters α and β defining the Fundamental Plane for The Three Hundred project galaxy clusters as a function of redshift. The results are shown for different temperature definitions and radial ranges (see inset). The dashed and dotted black lines indicate the virial expectation and the similarity solution for a secondary infall model, respectively.

and constant, implying that the CFP remains well defined throughout the evolution of the cluster population.

6 DYNAMICAL RELAXATION

During the growth history of individual haloes, the structural parameters of the NFW profile can be affected by the accretion of matter from their surroundings. The characteristic parameters r_{s} and M_{s} of individual clusters may thus change during its assembly. Then, the CFP may well be different between relaxed and unrelaxed clusters. Here, we investigate whether the CFP depends on the dynamical relaxation state of galaxy clusters (see Sections 4 and 5) using The Three Hundred project clusters.

For this purpose, we use the relaxation parameters defined in Cui et al. (2018): the virial ratio η, the centre-of-mass offset Δ_{r}, and the fraction of mass f_{s} (see Section 3.3 for their definitions). Following Cui et al. (2018), we assume that a cluster is dynamically relaxed when it satisfies that $0.85 < \eta < 1.15$, $\Delta_{\mathrm{r}} < 0.4$, and $f_{\mathrm{s}} < 0.1$. We note that these limiting values are defined inside r_{200}. To facilitate the simultaneous use of these three indicators, we combine them to define a new indicator or relaxation coefficient χ_{DS} (see equation 6), which is higher than unity for relaxed clusters.

We find that, overall, 37 per cent of the sample is dynamically relaxed ($\chi_{\mathrm{DS}} \geq 1$; see the bottom-right panel of Fig. 5). Although the fraction of relaxed and unrelaxed clusters changes according to the relaxation criteria employed and on the halo mass as shown in Cui et al. (2018), the sample contains more unrelaxed clusters than relaxed ones. The fraction of relaxed clusters increases with decreasing halo mass (see also Table 4 in Cui et al. 2018).
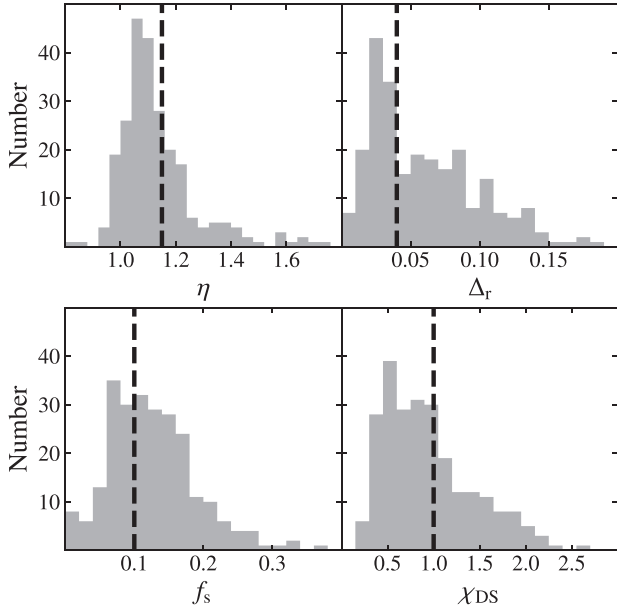
Figure 5. Distributions of the four dynamical relaxation indicators of The Three Hundred project clusters at $z = 0$. Upper panels: Virial ratio (η) and centre-of-mass offset (Δ_r). Lower panels: Fraction of mass in subhaloes (f_s) and the combination of the three parameters (χ_{DS}, see equation 6). The dashed lines show the threshold values for classification as 'relaxed' objects.

Table 4. Same as Table 3, but for the relaxed ($\chi_{DS} \geq 1$, upper panel) and unrelaxed ($\chi_{DS} \leq 2/3$, lower panel) subsamples.

$\chi_{DS} \geq 1$	α_1	α_0	β_1	β_0
$T_{mw}(500\,h^{-1}\,\mathrm{kpc})$	$-0.08^{+0.05}_{-0.06}$	$1.15^{+0.03}_{-0.02}$	$-0.25^{+0.10}_{-0.10}$	$-1.29^{+0.05}_{-0.06}$
$T_{mw}(r_{500})$	$-0.18^{+0.05}_{-0.06}$	$1.08^{+0.03}_{-0.03}$	$-0.34^{+0.10}_{-0.11}$	$-1.24^{+0.05}_{-0.06}$
$T_{mw}(r_{200})$	$-0.20^{+0.05}_{-0.05}$	$1.05^{+0.03}_{-0.02}$	$-0.41^{+0.10}_{-0.10}$	$-1.18^{+0.05}_{-0.05}$
$T_{sl}(500\,h^{-1}\,\mathrm{kpc})$	$-0.07^{+0.08}_{-0.09}$	$1.13^{+0.05}_{-0.03}$	$0.01^{+0.13}_{-0.14}$	$-1.26^{+0.07}_{-0.08}$
$T_{sl}(r_{500})$	$-0.14^{+0.07}_{-0.08}$	$1.11^{+0.04}_{-0.03}$	$-0.20^{+0.11}_{-0.12}$	$-1.31^{+0.06}_{-0.07}$
$T_{sl}(r_{200})$	$-0.20^{+0.07}_{-0.08}$	$1.14^{+0.05}_{-0.03}$	$-0.33^{+0.11}_{-0.12}$	$-1.40^{+0.07}_{-0.08}$
$\chi_{DS} \leq 2/3$	α_1	α_0	β_1	β_0
$T_{mw}(500\,h^{-1}\,\mathrm{kpc})$	$-0.14^{+0.11}_{-0.12}$	$1.18^{+0.07}_{-0.06}$	$-0.17^{+0.15}_{-0.15}$	$-1.40^{+0.09}_{-0.10}$
$T_{mw}(r_{500})$	$-0.15^{+0.09}_{-0.09}$	$1.05^{+0.05}_{-0.04}$	$-0.16^{+0.12}_{-0.12}$	$-1.22^{+0.06}_{-0.07}$
$T_{mw}(r_{200})$	$-0.03^{+0.11}_{-0.11}$	$0.98^{+0.05}_{-0.05}$	$-0.06^{+0.16}_{-0.16}$	$-1.11^{+0.08}_{-0.08}$
$T_{sl}(500\,h^{-1}\,\mathrm{kpc})$	$-0.35^{+0.11}_{-0.11}$	$1.28^{+0.07}_{-0.07}$	$-0.31^{+0.14}_{-0.14}$	$-1.58^{+0.10}_{-0.11}$
$T_{sl}(r_{500})$	$-0.33^{+0.10}_{-0.10}$	$1.18^{+0.06}_{-0.05}$	$-0.35^{+0.13}_{-0.13}$	$-1.51^{+0.08}_{-0.09}$
$T_{sl}(r_{200})$	$-0.40^{+0.10}_{-0.10}$	$1.26^{+0.07}_{-0.06}$	$-0.40^{+0.12}_{-0.13}$	$-1.59^{+0.09}_{-0.10}$

We find that relaxed and unrelaxed clusters at $z = 0$ (see Fig. 6) lie in well-defined regions of the CFP. Unrelaxed clusters exhibit, on average, higher values of r_s and M_s, whereas relaxed clusters typically have lower values of r_s and M_s, populating the opposite 'side' of the CFP. However, we do not find that The Three Hundred project clusters preferentially lie in a certain range of gas temperatures according to the degree of dynamical relaxation. These indicate that the CFP depends on the degree of dynamical relaxation of clusters, which should be explored in more detail. To this end, we split our sample of clusters into two subsamples according to the relaxation coefficient χ_{DS}. Hereafter, those clusters with $\chi_{DS} \geq 1$ are referred as relaxed systems, while those with $\chi_{DS} \leq 2/3$ are referred as unrelaxed systems.

6.1 The CFP of relaxed and unrelaxed clusters at $z = 0$

In our sample of 245 clusters at $z = 0$, there are 90 clusters with $\chi_{DS} \geq 1$. We repeat the analysis of CFP fitting using only relaxed clusters that are properly fitted by an NFW profile (i.e. $\sigma_{fit} \leq 2$). The results are summarized in Table A2 in Appendix A. We find that the CFP of relaxed clusters is closer to the expectation of simplified virial equilibrium ($\alpha = 1$ and $\beta = -1$), compared to the CFP obtained for the full sample (Section 4). This result is independent of the definition of weighted gas temperature and the radial ranged employed. In particular, the CFP parameters obtained using the mass-weighted temperature are compatible with $\alpha = 1$ and $\beta = -1$, even for the radial range of 500 h^{-1} kpc. For the spectroscopic-like temperature, we also find the same systematic differences with respect to the results obtained for the full sample (Section 4). The α parameter is typically smaller by $\sim 0.06 \pm 0.03$ than for the full sample, while the β parameter is larger (less negative) by $\sim 0.15 \pm 0.04$ than for the full sample (see Tables 2 and A2). The thickness of the CFP of relaxed clusters is also systematically smaller than obtained for the full sample by down to 0.005 dex (see Table A2 in Appendix A).

Regarding the unrelaxed subsample, there are 87 clusters with $\chi_{DS} \leq 2/3$ at $z = 0$. The trends in the changes in α and β are opposite to those for the relaxed subsample (see Table A2 in Appendix A). Overall, except for the mass-weighted temperatures within r_{500} and r_{200}, α slightly increases by 0.10 ± 0.05, while β decreases by 0.15 ± 0.05. It is remarkable that for the mass-weighted temperatures within r_{500} and r_{200}, α and β are close to virial expectations.

We find that β is the CFP parameter most sensitive to the relaxation classification (see Table A2 in Appendix A). The CFP of unrelaxed clusters is halfway between the virial expectation and the similarity solution. It should be noted that for the spectroscopic-like temperature with the 500 h^{-1} kpc radial range, the α and β values are close to the similarity solution ($\alpha = 1.5$ and $\beta = -2$). As expected, the thickness of the CFP for the unrelaxed subsample is slightly larger than obtained for the full sample and the relaxed subsample. Hence, although clusters systematically move across the ($\log M_s$, $\log r_s$, $\log T$) space during their evolution, the mass growth of clusters can slightly tilt the CFP and increase the dispersion of this plane.

6.2 Redshift evolution of the CFP for relaxed and unrelaxed clusters

Here, we explore the evolution of the CFP with redshift for relaxed and unrelaxed clusters separately. To this end, we use The Three Hundred project clusters identified at different epochs (Section 5) and at each redshift we split them into relaxed and unrelaxed subsamples according to our relaxation criteria ($\chi_{DS} \geq 1$ and $\chi_{DS} \leq 2/3$, respectively). Specifically, we derive the CFP for each subsample at $z = 0.07$, 0.22, 0.33, 0.59, and 0.99. We note that the relaxation parameter χ_{DS} for each individual cluster is recomputed within r_{200} at each redshift, so that some clusters identified as relaxed at $z = 0$ may be identified as unrelaxed at higher redshifts, and vice versa. As in Section 5, the redshift evolution of the CFP parameters $\alpha(z)$ and $\beta(z)$ is parametrized as $\alpha(z) = \alpha_0 (1 + z)^{\alpha_1}$ and $\beta(z) = \beta_0 (1 + z)^{\beta_1}$.

There are more (fewer) relaxed (unrelaxed) clusters at $z = 0$ than at $z = 1$, all selected to have $\sigma_{fit} \leq 2$. We find that the redshift evolution of α and β for the relaxed subsample is milder than for the unrelaxed subsample (see Fig. 7 and Table 4). Moreover, the CFP parameters α and β for the relaxed subsample are closer to the virial expectation at all redshifts probed. On the other hand, the unrelaxed subsample exhibits a stronger evolution for the spectroscopic-like temperature
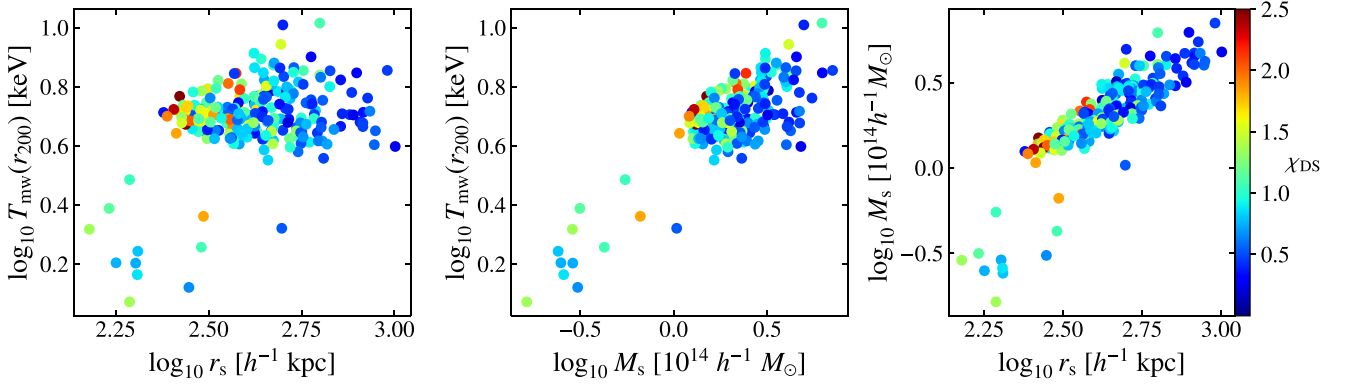
Figure 6. Distribution of the dynamical relaxation parameter χ_{DS} (see equation 6) in three projections of the ($\log_{10}M_s$, $\log_{10}r_s$, and $\log_{10}T$) space for The Three Hundred project clusters at $z = 0$. Redder (bluer) colours correspond to relaxed (unrelaxed) clusters.
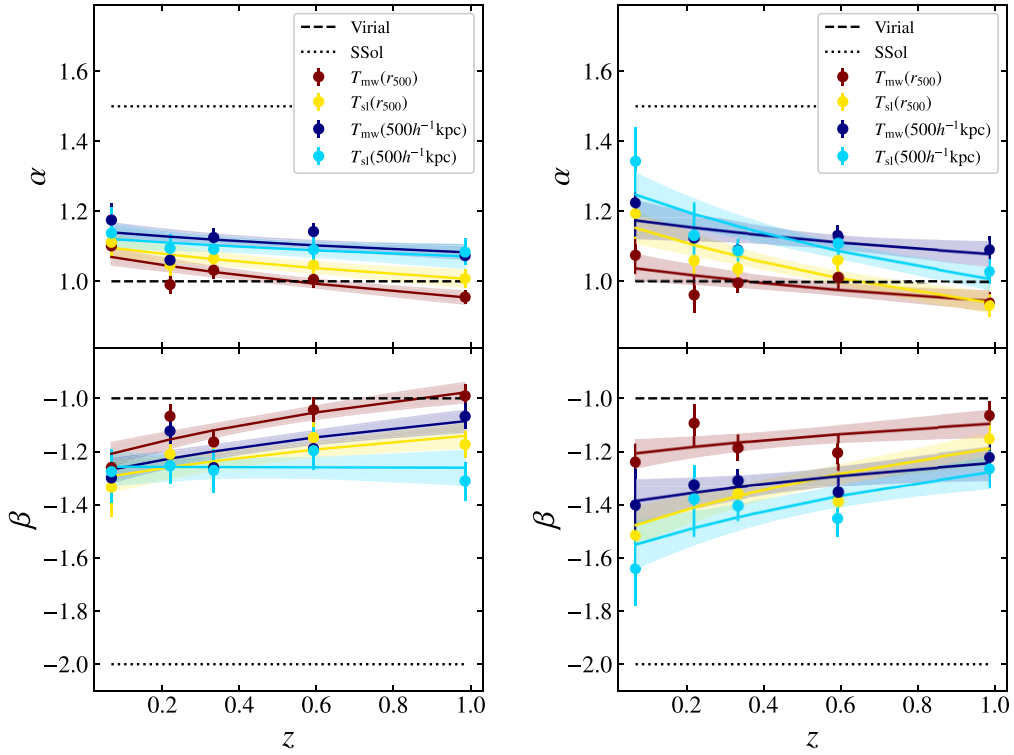

Figure 7. Same as Fig. 4, but for relaxed and unrelaxed clusters (left- and right-hand panels, respectively).

case. The CFP at $z \sim 1$ is close to the virial expectation as found in Section 5. However, the absolute values of α and β for the unrelaxed subsample increase progressively towards lower redshifts (see the right-hand panel of Fig. 7), coming closer to the similarity solution for a secondary infall model. Our results thus suggest that relaxed and unrelaxed clusters qualitatively evolve in a similar manner (growing α and decreasing β towards $z = 0$), but with different amplitude.

6.3 Dependence of the CFP on the formation redshift

The formation redshift of clusters z_{form}, defined as the time when the mass reaches half of the value at $z = 0$ [$M_{200}(z_{form}) = 0.5M_{200}(z = 0)$], is linked to their mass assembly history and dynamical relaxation state. Clusters formed earlier have had more time to relax and have likely already transitioned from the fast to slow accretion phase,

when the halo growth mostly occurs in their outskirts and r_s remains approximately constant. Mostoghiu et al. (2019) found that relaxed and unrelaxed clusters at $z = 0$ from The Three Hundred project have different distributions of z_{form}. On average, relaxed clusters at $z = 0$ have higher z_{form} compared to unrelaxed clusters. Using The Three Hundred project clusters at $z = 0$ selected to have $\sigma_{fit} \leq 2$, we explore the CFP in three bins of formation redshift: $z_{form} < 0.4$, $0.4 \leq z_{form} < 0.6$, and $z_{form} \geq 0.6$. The results are summarized in Table A3 in Appendix A.

Clusters that formed earlier, $z_{form} \geq 0.6$, and thus those that are likely in the slow accretion phase, form a CFP at $z = 0$ that is deviated from the similarity solution for a secondary infall model (see Table A3 in Appendix A). This conclusion applies to all temperature definitions and radial ranges explored in this work. In particular, the results obtained for the $z_{form} \geq 0.6$ subsample using the mass-

weighted temperature are fairly consistent with the expectation for simplified virial equilibrium ($\alpha = 1$ and $\beta = -1$). It should be noted that we find qualitatively similar results for relaxed clusters (see Table A2 in Appendix A). This is not surprising, since clusters classified as relaxed ($\chi_{DS} \geq 1$) exhibit typical formation redshifts of $z_{form} > 0.4$, although there are some unrelaxed clusters ($\chi_{DS} \leq 2/3$) with $z_{form} \geq 0.6$ and some relaxed clusters ($\chi_{DS} \geq 1$) with $z_{form} < 0.6$. The CFP parameters obtained with the spectroscopic-like temperature are slightly closer to the similarity solution compared to those with the mass-weighted temperature.

On the other hand, the CFP parameters obtained for recently formed clusters with $z_{form} < 0.4$ ($\alpha \sim 1.25$ and $\beta \sim -1.5$; see Table A3) lie halfway between the simplified virial expectation and the similarity solution. In particular, the results obtained with $T_{sl}(500\,h^{-1}\,\mathrm{kpc})$ are compatible with the similarity solution. These findings are in line with the results for the subsample of unrelaxed clusters ($\chi_{DS} \leq 2/3$). This is a natural consequence of the fact that all The Three Hundred project clusters with $z_{form} < 0.4$ have $\chi_{DS} < 1$ (see also Table A2 in Appendix A).

For the subsample of intermediate-z_{form} clusters with $0.4 \leq z_{form} < 0.6$, we find CFP parameters that are consistent with the $z_{form} \geq 0.6$ subsample within the 1σ uncertainty level (see Table A3 in Appendix A). This suggests that the dependence of the CFP on the formation epoch only comes into play for the most recently formed clusters with $z_{form} < 0.4$, or equivalently, those clusters formed over the last ~ 4 Gyr.

Consequently, there are hints pointing out that the CFP of recently formed clusters differs from that of clusters assembled at higher redshift. This conclusion holds irrespective of the definition and radial range of weighted temperature, at a significance level higher than 1σ in all cases. The typical differences between the CFP parameters of clusters with $z_{form} < 0.4$ and $z_{form} \geq 0.6$ are approximately $\Delta\alpha \sim 0.21 \pm 0.03$ and $\Delta\beta \sim -0.26 \pm 0.05$. The largest discrepancy between these two subsamples is found when the CFP is defined using the innermost region of clusters (i.e. $r \leq 500\,h^{-1}\,\mathrm{kpc}$) to compute the weighted temperature, where the differences in the CFP parameters are of the order of $\Delta\alpha \sim 0.45 \pm 0.12$ and $\Delta\beta \sim -0.53 \pm 0.18$. Moreover, the CFP thickness of $z_{form} < 0.4$ clusters is larger than for clusters formed at higher redshift. This reflects that recently formed clusters tend to have disturbed internal structures, which increases the dispersion of the CFP.

7 FUNDAMENTAL PLANE OF CLASH CLUSTERS

Making use of the CLASH data sets, we have also explored the Fundamental Plane obtained from observations. In this study, we re-analysed the 20 CLASH clusters of Fujita et al. (2018a, b) by adopting the methodology described in Section 3. For the CLASH sample, we used X-ray temperatures measured in the radial range 50–$500\,h^{-1}\,\mathrm{kpc}$ (see Section 2.2).

We find that the CLASH sample lies on a plane in logarithmic space defined by (M_s, r_s, and T_X), as previously found by Fujita et al. (2018a). The best-fitting parameters of α, β, and δ obtained with MINDISQ (shown in Table 5 and Fig. 8) provide the CFP with the lowest dispersion ($\sigma_d = 0.037$ dex) and these results are compatible with those obtained by Fujita et al. (2018a):

$$T_X \propto M_s^{1.93^{+0.81}_{-0.57}}\, r_s^{-2.57^{+0.83}_{-1.14}} \sim M_s^{1.9}\, r_s^{-2.6}. \tag{9}$$

We find that the discrepancies between the Fundamental Planes obtained for clusters of The Three Hundred project and those from

CLASH are mainly due to the clusters with the highest X-ray temperatures. The rest of clusters lie on a shared region between both Fundamental Planes.

In addition, we explore whether the Fundamental Plane can be affected by the inclusion of unrelaxed clusters, even though the sample size is reduced. To this end, we removed those clusters identified as unrelaxed candidates in Postman et al. (2012; see Table 1). This results in a subsample of 13 CLASH clusters. For this 'relaxed' subsample, we find that the resulting CFP is compatible with both the virial expectation and the similarity solution within the increased uncertainty, as shown in Table 5. Instead, if we exclude the four hottest clusters with $T_X > 12$ keV (RX J2248.7$-$4431, RX J1347.5$-$1145. MACS J0717.5+3745l, and MACS J0647.7+7015), the CFP of the CLASH sample comes closer to the virial expectation, while the uncertainties of the CFP parameters decrease (see Table 5 and right-hand panel in Fig. 8). Hence, the four hottest clusters appear to be systematically deviated from the plane defined by the rest of the CLASH sample.

The CFP obtained for a relaxed sample of The Three Hundred project clusters ($\chi_{DS} \geq 1$) can be compared to the CLASH sample at a median redshift of $z \sim 0.35$. Using the spectroscopic-like temperature $T_{sl}(500\,h^{-1}\,\mathrm{kpc})$, the CFP parameters for the relaxed simulated sample at $z = 0.35$ are obtained as $\alpha = 1.10 \pm 0.02$ and $\beta = -1.26 \pm 0.04$ (see Section 6.2 and Table 4). This is in agreement with the CFP parameters (α, β) obtained for a subsample of CLASH clusters with T_X lower than 12 keV (see Table 5), above which no simulated clusters are found. Two of the four hottest CLASH clusters (MACS J0717.5+3745 and MACS J0647.7+7015) are high-magnification-selected systems at $z > 0.5$, which often turn out to be dynamically disturbed, highly massive ongoing mergers (Torri et al. 2004; Meneghetti et al. 2010, 2014, 2020; Umetsu 2020). The other two (RX J2248.7$-$4431 and RX J1347.5$-$1145) are X-ray-selected clusters that are classified as unrelaxed. The inclusion of the four clusters with $T_X > 12$ keV alters the CFP for CLASH, in such a way that the CFP becomes compatible with the similarity solution. Here the main point is that these four clusters lie on the upper side of the CFP, so that they have a high contribution to determining the CFP for CLASH. This result suggests the possibility that the inclusion of clusters undergoing transient merger-induced boosts in temperature (Ricker & Sarazin 2001) can significantly affect the inference of the CFP parameters.

8 DISCUSSION

This section is devoted to a discussion of our findings from The Three Hundred project simulations. In Sections 8.1 and 8.2, we explore potential sources of systematic effects that could bias our determination of the CFP. In Section 8.3, we analyse simulated cluster data in the published literature to derive their cluster Fundamental Planes (CFP) and compare them with our results from The Three Hundred project simulations.

8.1 Robustness of the NFW fitting procedure

Here, we study systematic effects on the determination of the characteristic halo parameters r_s and M_s and their impact on the resulting CFP. Specifically, we investigate how the CFP parameters depend on the NFW fitting procedure using The Three Hundred project simulations.

To study possible effects of the choice of the fitting range, we repeat NFW fits using different radial ranges. For clusters at $z = 0$, we refit the NFW formula to mass profiles $M(< r)$ of individual

Table 5. Best-fitting parameters (α, β, and δ) and thickness (σ_d in dex units) of the Fundamental Plane (see equation 7) derived for the CLASH sample. The upper and lower errors enclose the 1σ uncertainty range. The normalization parameters ($M_{s,0}$, $r_{s,0}$, and $T_{X,0}$) are also included in the table for each case.

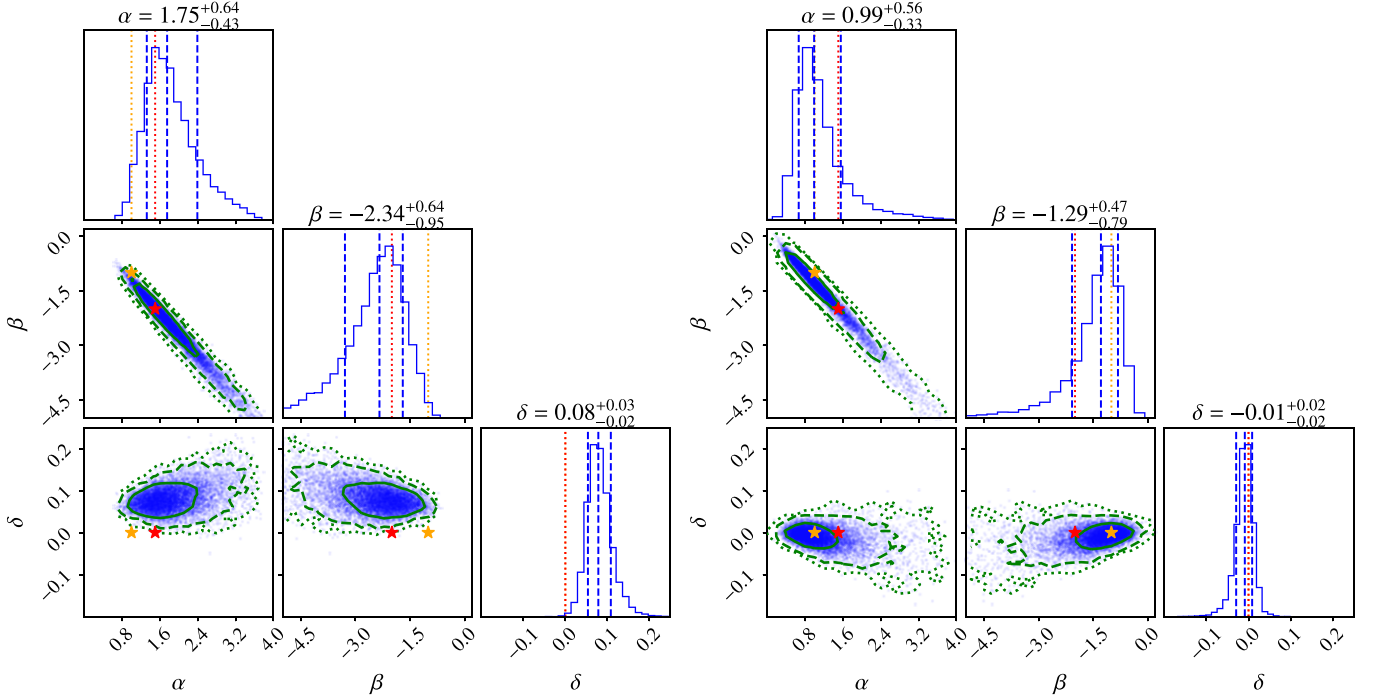|	Number	α	β	δ	σ_d (dex)	$M_{s,0}$ ($10^{14}\,h^{-1}\,M_\odot$)	$r_{s,0}$ (h^{-1} kpc)	$T_{X,0}$ (keV)
CLASH	20	$1.75^{+0.64}_{-0.43}$	$-2.34^{+0.64}_{-0.95}$	$0.078^{+0.030}_{-0.024}$	0.037	2.96	407	7.75
CLASH relaxed	13	$1.82^{+0.86}_{-0.64}$	$-2.45^{+0.96}_{-1.28}$	$0.135^{+0.056}_{-0.039}$	0.029	2.38	354	6.70
CLASH ($T_X < 12$ keV)	16	$0.99^{+0.56}_{-0.33}$	$-1.29^{+0.47}_{-0.79}$	$-0.009^{+0.017}_{-0.021}$	0.032	2.54	399	7.40

Figure 8. Constraints on the parameters defining the Fundamental Plane (see equation 7) of CLASH galaxy clusters. Green solid, dashed, and dotted lines illustrate the confidence levels of 68, 95, and 99.7 per cent of probability, respectively. Dashed blue lines show the 16th, 50th, and 84th percentiles of the distributions of parameters obtained from the posterior distributions of the NFW parameters for all individual clusters. The orange and red star-shaped symbols, as well as orange and red dotted lines in the histograms, indicate the virial expectation and the similarity solution for a secondary infall model, respectively.

clusters in the radial range from $0.08 \times r_{100}$ to $2\,h^{-1}$ Mpc. For clusters at higher redshifts ($z = 0.07, 0.22, 0.33, 0.59$, and 0.99), we perform NFW fits in the radial range from $0.1 \times r_{200}$ to $2\,h^{-1}$ Mpc.

We also repeat NFW fits using the density profile $\rho(r)$, instead of the mass profile $M(<r)$. We fit the NFW model (equation 1) to density profiles of individual clusters to determine r_s and M_s in two different radial ranges, namely: $[0.08, 1.0] \times r_{100}$ and from $0.08 \times r_{100}$ to $2\,h^{-1}$ Mpc for clusters at $z = 0$. For clusters at higher redshifts ($z = 0.07, 0.22, 0.33, 0.59$, and 0.99), we perform NFW fits to density profiles in radial ranges of $[0.1, 1.0] \times r_{200}$ and from $0.1 \times r_{200}$ to $2\,h^{-1}$ Mpc.

With new sets of r_s and M_s, we have repeated our CFP analysis, focusing on the dependence of the CFP on different temperature definitions, the redshift evolution of the CFP, and its dependence on the dynamical state of clusters. As a result, we find no evidence of significant differences in the CFP parameters when using different NFW fitting procedures for extracting the r_s and M_s parameters. Therefore, our main conclusions remain unchanged. We only find mild discrepancies typically amounting to $|\Delta\alpha|$, $|\Delta\beta| \lesssim 0.1$.

8.2 Robustness of the $\sigma_{\rm fit}$ selection

To study the CFP, we constructed a simulated cluster sample from The Three Hundred project by selecting haloes according to the fitting quality of the NFW profile, $\sigma_{\rm fit} = \chi^2/{\rm dof} \leq 2$. This selection is to remove from the analysis those clusters that are not properly described by an NFW profile owing to the presence of strong asymmetries and massive substructures associated with mergers. It should be noted that, however, cosmological N-body simulations of ΛCDM reveal systematic deviations of quasi-equilibrium density profiles of collisionless haloes from the self-similar NFW form (e.g. Navarro et al. 2004; Merritt et al. 2006). These numerical studies found that the density profiles of CDM haloes are generally better fitted by a three-parameter Einasto profile, while both NFW and Einasto profiles describe well the density profiles of cluster-scale haloes at low redshifts ($z < 1$; Child et al. 2018), as found by cluster-lensing observations (e.g. Umetsu et al. 2016). Although the NFW assumption is well justified for our CFP analysis of cluster-scale CDM haloes at $z < 1$, we examine here the robustness of our findings
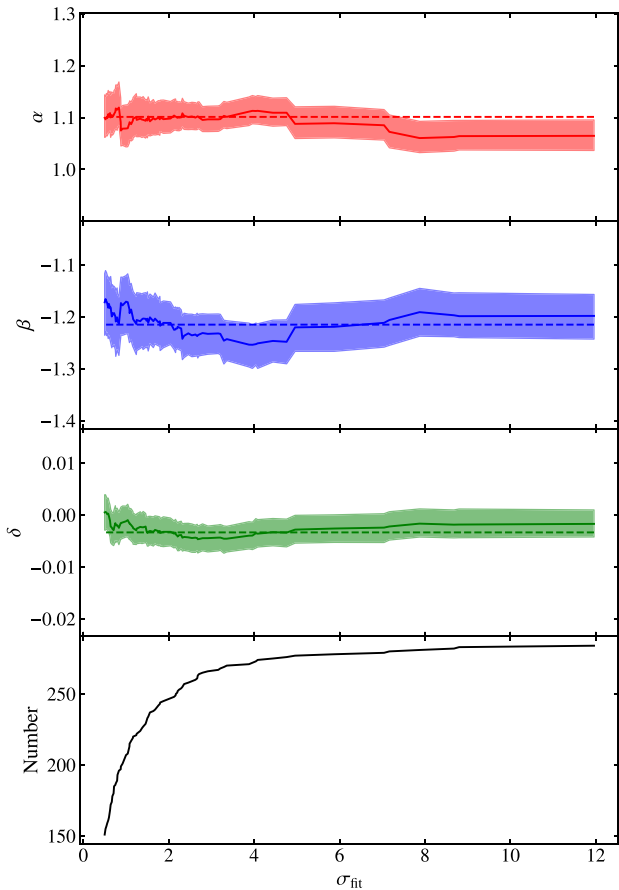
Figure 9. Best-fitting parameters describing the Fundamental Plane at $z = 0$ (see equation 7) as a function of the $\sigma_{\rm fit}$ threshold obtained for The Three Hundred project clusters using the mass-weighted temperature within $500\,h^{-1}$ kpc. From top to bottom: α, β, δ, and number of clusters included in the analysis. In each panel, the shaded area shows the 1σ uncertainty range obtained by a bootstrapping technique. The dashed lines show the best-fitting parameters for $\sigma_{\rm fit} \leq 2$.

as a function of the $\sigma_{\rm fit}$ threshold using The Three Hundred project simulations.

To this end, we repeat our CFP analysis for about 80 values of the $\sigma_{\rm fit}$ threshold, ranging from 0.5 up to 12. About half of The Three Hundred project clusters at $z = 0$ have $\sigma_{\rm fit}$ values below 0.5, so that a good fraction of our simulated clusters are properly fitted by an NFW profile. On the other hand, less than 15 per cent of the clusters have $\sigma_{\rm fit} > 3$, and less than 8 per cent present $\sigma_{\rm fit} > 5$.

Overall, we find that the resulting CFP parameters (α, β, and δ) obtained for all cases at $z = 0$ are independent of the $\sigma_{\rm fit}$ threshold and consistent within the 1σ uncertainty level, up to the $\sigma_{\rm fit}$ threshold of 6. Here, the relative change in the CFP parameters is below 3–4 per cent in all cases. This change in the parameters increases up to 8 per cent, which corresponds to the selection threshold of $\sigma_{\rm fit} \leq 12$ for the spectroscopic-like temperature within $500\,h^{-1}$ kpc. In Fig. 9, we show the CFP parameters α, β, and δ as a function of the $\sigma_{\rm fit}$ threshold.

We have also performed this test for The Three Hundred project clusters at $z > 0$, finding that the relative change in the CFP parameters (α, β, and δ) decreases with increasing redshift. At $z = 0.99$, the change in the CFP parameters is negligible regardless of

the $\sigma_{\rm fit}$ threshold, even when including all clusters independently of the NFW fitting quality.

Finally, we also checked the stability of our results against the inclusion of clusters with extreme $\sigma_{\rm fit}$ values, namely, those with $\sigma_{\rm fit} \leq 0.05$ and $\sigma_{\rm fit} \geq 2$. We find that these are homogeneously distributed across the range of the parameters explored in The Three Hundred project and they do not preferentially populate particular regions of the Fundamental Plane. We thus conclude that our simulation results do not depend on the particular choice of the $\sigma_{\rm fit}$ threshold.

8.3 Fundamental Planes from other cluster simulations

The central gas properties in galaxy clusters and their connection with the dark-matter potential are sensitive to the effect of baryonic feedback. Hence, different implementations of baryonic physics in cosmological cluster simulations, as well as different cluster selection procedures, may lead to different predictions of the CFP. In this subsection, we confront our findings with those obtained from the adiabatic MUSIC *N*-body/hydrodynamical simulations (Meneghetti et al. 2014, Section 8.3.1) and another set of simulation data including non-gravitational feedback detailed in Rasia et al. (2015); Planelles et al. (2017, hereafter FB simulations; Section 8.3.2). It is of note that these simulations were also used to explore the CFP in Fujita et al. (2018a).

8.3.1 MUSIC simulations

The MUSIC sample consists of resimulated haloes selected from the dark-matter-only suit of MultiDark simulations ($\Omega_{\rm M} = 0.27$, $\Omega_{\rm b} = 0.0469$, $\Omega_{\Lambda} = 0.73$, $\sigma_8 = 0.82$, $n_{\rm s} = 0.95$, and $h = 0.7$), whose haloes are more massive than $10^{15}\,h^{-1}\,{\rm M}_\odot$ at $z = 0$. For the high-resolution resimulation of Lagrangian regions around haloes (a spherical region with radius of $6\,h^{-1}$ Mpc at $z = 0$), the TREEPM + SFH GADGET code (Springel 2005) was used, reaching a mass resolution for dark matter and gas of $m_{\rm DM} = 9.01 \times 10^8\,h^{-1}\,{\rm M}_\odot$ and $m_{\rm gas} = 1.9 \times 10^8\,h^{-1}\,{\rm M}_\odot$, respectively. The MUSIC simulations do not include any non-gravitational effects, such as AGN and supernova feedback, and there is no radiative cooling implemented.

Following Fujita et al. (2018a), we select all MUSIC clusters with $M_{200} > 2 \times 10^{14}\,h^{-1}\,{\rm M}_\odot$ at $z = 0.25$ regardless of their dynamical state, amounting a total of 402 clusters. Mass-weighted temperatures were computed for these clusters within the r_{500} radial range, without excluding the core region (Fujita et al. 2018a). This decision is based on that the MUSIC sample does not present cool-core features because the MUSIC simulations are non-radiative. The CFP of MUSIC clusters and the uncertainties in the CFP parameters are computed following the methodology described in Section 3.5. For this sample, however, it is not possible to remove clusters that are not properly fitted by an NFW profile (i.e. no $\sigma_{\rm fit}$ selection applied) and the only temperature employed is $T_{\rm mw}(r_{500})$.

We find that the CFP of MUSIC clusters is characterized by $\alpha = 1.28^{+0.03}_{-0.02}$ and $\beta = -1.55^{+0.05}_{-0.05}$ (see Table 6 and Fig. 10), which lie between the simplified virial expectation ($\alpha = 1$, $\beta = -1$) and the similarity solution for a secondary infall model ($\alpha = 1.5$, $\beta = -2$). In contrast, we find $\alpha = 1.00^{+0.02}_{-0.02}$ and $\beta = -1.12^{+0.03}_{-0.03}$ for The Three Hundred project clusters at $z = 0.22$ using the same temperature definition (see Table A1 in Appendix A), which is closer to the simplified virial expectation and significantly different from the MUSIC results at $z = 0.25$. Moreover, the CFP obtained with the MUSIC simulations has a larger dispersion of $\sigma_{\rm d} = 0.023$ dex, compared to $\sigma_{\rm d} = 0.018$ dex for The Three Hundred

Table 6. Best-fitting parameters (α, β, and δ) and thickness (σ_d in dex units) of the Fundamental Plane obtained for simulated cluster samples, MUSIC at $z = 0.25$, FB0 at $z = 0$, and FB1 at $z = 1$. The lower and upper errors enclose the 1σ uncertainty.

|	Number	α	β	δ	σ_d (dex)	$M_{s,0}$ ($10^{14}\,h^{-1}\,M_\odot$)	$r_{s,0}$ (h^{-1} kpc)	T_0 (keV)
MUSIC $T_{mw}(r_{500})$	402	$1.28^{+0.03}_{-0.02}$	$-1.55^{+0.05}_{-0.05}$	$0.02^{+0.00}_{-0.00}$	0.023	0.97	283	3.68
FB0 $T_{mw}(500\,h^{-1}$ kpc)	29	$1.36^{+0.12}_{-0.10}$	$-1.88^{+0.20}_{-0.25}$	$-0.07^{+0.01}_{-0.01}$	0.027	2.07	444	7.91
FB0 $T_{mw}(r_{500})$	29	$1.25^{+0.09}_{-0.08}$	$-1.66^{+0.16}_{-0.20}$	$-0.06^{+0.01}_{-0.01}$	0.022	2.07	444	6.73
FB0 $T_{sl}(500\,h^{-1}$ kpc)	29	$1.32^{+0.15}_{-0.13}$	$-1.84^{+0.27}_{-0.32}$	$-0.07^{+0.02}_{-0.02}$	0.030	2.07	444	7.13
FB0 $T_{sl}(r_{500})$	29	$1.19^{+0.08}_{-0.06}$	$-1.62^{+0.12}_{-0.15}$	$-0.07^{+0.01}_{-0.01}$	0.016	2.07	444	6.61
FB1 $T_{mw}(500\,h^{-1}$ kpc)	29	$1.29^{+0.14}_{-0.12}$	$-1.87^{+0.35}_{-0.34}$	$0.02^{+0.02}_{-0.02}$	0.034	0.47	187	3.27
FB1 $T_{sl}(500\,h^{-1}$ kpc)	29	$1.17^{+0.13}_{-0.11}$	$-1.69^{+0.34}_{-0.33}$	$0.05^{+0.02}_{-0.02}$	0.030	0.47	187	2.97
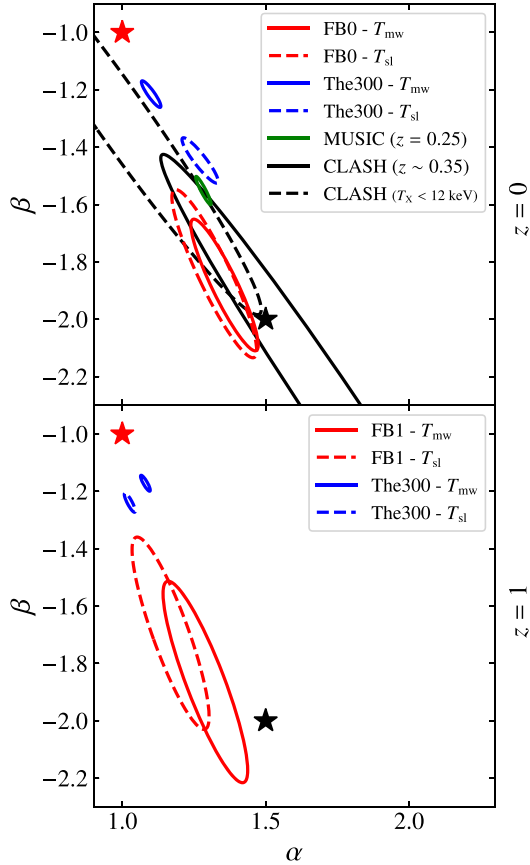
Figure 10. Constraints on the parameters α and β defining the CFP at $z = 0$ obtained for The Three Hundred project and FB simulations (top panel, blue and red lines, respectively) using mass-weighted and spectroscopic-like temperatures measured within $500\,h^{-1}$ kpc (solid and dashed lines, respectively). The contours show the 68 per cent confidence intervals in the α–β plane. The results obtained for the MUSIC simulations (green line) and CLASH (black lines), as well as the expectations for simplified virial equilibrium (red filled star) and the similarity solution for a secondary infall model (black filled star), are also shown. Similarly, the constraints on (α, β) at $z = 1$ for The Three Hundred project and FB simulations are shown in the bottom panel.

project simulations. The main difference between the MUSIC and The Three Hundred project simulations is the implementation of non-gravitational feedback (see Section 2.1), meaning that both supernova feedback and AGN feedback were not implemented in the former set

of simulations. This may suggest that quantitative predictions of the CFP depend on the implementation of non-gravitational physics to some degree.

8.3.2 FB0 and FB1 simulations

The FB simulation sample consists of 29 massive haloes with $M_{200} \in [1$–$30] \times 10^{14}\,h^{-1}\,M_\odot$ at $z = 0$, selected from a parent N-body cosmological simulation ($\Omega_M = 0.24$, $\Omega_b = 0.04$, $\Omega_\Lambda = 0.76$, $\sigma_8 = 0.8$, $n_s = 0.96$, and $h = 0.72$; see Rasia et al. 2015; Planelles et al. 2017). Lagrangian regions around the selected clusters were resimulated with an improved resolution to include the baryonic component in hydrodynamic simulations. These simulations were carried out with the GADGET code, including an updated SPH scheme detailed in Beck et al. (2016), reaching a final mass resolution of $m_{DM} = 8.47 \times 10^8\,h^{-1}\,M_\odot$ and $m_{gas} = 1.53 \times 10^8\,h^{-1}\,M_\odot$ for the dark matter and gas components, respectively. The FB simulations include baryonic feedback effects, such as radiative cooling, star formation, supernova feedback, and metal enrichment, as well as AGN feedback (for further details, see Rasia et al. 2015; Planelles et al. 2017). We note that the code used to perform The Three Hundred project simulations is essentially the same as for the FB simulations, where the main differences are certain choices in stellar evolution and AGN feedback, as well as in the resimulated regions.

For our analysis, we select from Fujita et al. (2018a) all 29 clusters for the simulation runs at $z = 0$ and $z = 1$ (hereafter FB0 and FB1, respectively). Since this set of simulations includes radiative processes, mass-weighted and spectroscopic-like temperatures were computed within core-excised regions of $r \in [50, 500] \times h^{-1}$ kpc and $[0.15, 1.0] \times r_{500}$ (Fujita et al. 2018a). For the FB1 run, both weighted temperatures are measured in the $[50, 500] \times h^{-1}$ kpc radial range. We have repeated our CFP analysis on the FB cluster sample at $z = 0$ and $z = 1$ following the procedure described in Section 3.5. It is worth mentioning that we used the same simulated sample than in Fujita et al. (2018a) to explore the CFP by simulated clusters, where the only difference was the analysis outlined in Section 3.5.

For the FB0 run, we find the best-fitting CFP parameters in the range $\alpha \in [1.19, 1.36]$ and $\beta \in [-1.62, -1.88]$ (see Table 6). The best-fitting α and β parameters lie halfway between the simplified virial expectation and the similarity solution for a secondary infall model. These results are compatible with the similarity solution within a 95 per cent uncertainty level (see Fig. 10). We find no evidence of discrepancies between the results obtained using the spectroscopic-like and mass-weighted temperatures. We note that for the FB simulations, the uncertainties on the CFP parameters are typically larger owing to the small sample size of simulated clusters.

For The Three Hundred project simulations, we find a tendency that the absolute values of α and β decrease with increasing aperture radius within which the weighted temperature is computed (see Table 6).[3] The absolute values of α and β obtained for the FB0 sample are systematically larger than the corresponding The Three Hundred project results (see Table 2). Overall, the dispersion of the CFP for the FB0 sample is comparable to, but in some cases larger than, the corresponding The Three Hundred project results.

For the FB1 run, we find a similar set of α and β values to the FB0 results (Table 6). Comparing the FB0 and FB1 results, we find that there is a slight evolution of the CFP parameters, thus leading to similar conclusions. In particular, we notice that the CFP parameters (α, and β) for the FB1 sample are slightly less compatible with the similarity solution compared to the FB0 case. The variations in the CFP parameters are still compatible with no evolution given the large uncertainties. Nevertheless, the trends are qualitatively consistent with The Three Hundred project results (see Section 5). Overall, the absolute values of α and β increase with decreasing redshift, coming closer to the similarity solution.

9 SUMMARY AND CONCLUSIONS

Recent observational studies (Fujita et al. 2018a, b) suggested that galaxy clusters form a tight Fundamental Plane in logarithmic space of the gas temperature (T) and the characteristic halo scale radius and mass (r_s and M_s), that is, $T \propto M_s^\alpha r_s^\beta$. This CFP was found to deviate from the virial equilibrium expectation, $T \propto M_s r_s^{-1}$, and to be in better agreement with the similarity solution for a secondary infall model (Bertschinger 1985), $T \propto M_s^{1.5} r_s^{-2}$.

In this paper, we have carried out a systematic study of the CFP using a sample of ~250 simulated clusters from The Three Hundred project (Cui et al. 2018). In particular, we focus on the stability of the plane with different temperature definitions and its dependence on the dynamical relaxation state of clusters. The characteristic scale parameters of The Three Hundred project clusters, r_s and M_s, were extracted from the total mass profiles $M(< r)$ of individual clusters assuming an NFW halo description. After excluding clusters with poor fit quality of the NFW profile ($\sigma_{\rm fit} = \chi^2/{\rm dof} > 2$), we have 245 clusters in our sample at $z = 0$. At higher redshifts ($z = 0.07, 0.22, 0.33, 0.59$, and 0.99), the number of selected clusters ranges from 231 to 280. We have explored two definitions of weighted temperatures, namely mass-weighted and spectroscopic-like temperatures ($T_{\rm mw}$ and $T_{\rm sl}$), and computed them in three radial ranges: $[0.1, 1.0] \times r_{200}$, $[0.15, 1.0] \times r_{500}$, and $[50, 500] \times h^{-1}$ kpc.

We find that The Three Hundred project clusters at $z = 0$ lie on a thin plane whose parameters (α and β) and dispersion ($\sigma_d = 0.015$–0.030 dex) depend on the gas temperature definition (Section 4, Table 2, and Figs 2 and 3). Overall, the resulting CFP parameters are found in the range $1 < \alpha < 1.5$ and $-2 < \beta < -1$, that is, the range bounded by the virial equilibrium expectation and the similarity solution. The CFP for mass-weighted temperatures is slightly closer to the virial expectation ($\alpha = 1$, $\beta = -1$) with a smaller dispersion, whereas the CFP parameters for the spectroscopic-like temperature lie halfway values between the virial expectation and the similarity solution. When gas temperatures are measured within $500\ h^{-1}$ kpc, which is close to the median value of r_s for The Three Hundred project sample, the resulting CFP deviates the most from the virial

expectation and shifts towards the similarity solution ($\alpha = 1.5$, $\beta = -2$).

We have explored the evolution of the CFP with redshift for relaxed and unrelaxed clusters separately (Section 6). Independently of the temperature definition, we find that clusters at $z = 1$ form a CFP similar to the virial expectation, which evolves into a CFP that is halfway between the virial expectation and the similarity solution (Table 4 and Fig. 7). For the unrelaxed subsample, the absolute values of α and β progressively increase towards lower redshifts, coming closer to the similarity solution. In contrast, the CFP of relaxed clusters remains close to the virial expectation, with a milder evolution than for the unrelaxed subsample. Importantly, at all epochs, the CFP remains well defined throughout the evolution of the cluster population.

We have also studied the dependence of the CFP on the formation redshift, $z_{\rm form}$, using The Three Hundred project clusters at $z = 0$ (Section 6.3). Our results suggest that the CFP of recently formed clusters ($z_{\rm form} < 0.4$) differs from that of clusters assembled at higher redshift, independently of the temperature definition (Table A3 in Appendix A). We find that clusters with $z_{\rm form} < 0.4$ form a CFP at $z = 0$ that is most deviated from the virial expectation. In particular, the results obtained with the spectroscopic-like temperature within $500\ h^{-1}$ kpc are compatible with the similarity solution. These findings are in line with the results for the unrelaxed subsample. In fact, we verify that all The Three Hundred project clusters with $z_{\rm form} < 0.4$ are classified as unrelaxed.

Making use of the multiwavelength CLASH data sets, we also examined the Fundamental Plane for real clusters (Section 7). We find that the CLASH sample forms a CFP with $\alpha = 1.93^{+0.81}_{-0.57}$ and $\beta = -2.57^{+0.83}_{-1.14}$, with a dispersion of $\sigma_d = 0.037$ dex (see Table 5 and left-hand panel in Fig. 8). The results are compatible with those obtained by Fujita et al. (2018a) using the same data but with a different fitting procedure for the CFP measurement. There is a slight discrepancy between the Fundamental Planes obtained for clusters in The Three Hundred project and the CLASH sample (Fig. 10). We find that the inclusion of the four hottest clusters with $T_X > 12$ keV alters the CFP for CLASH. Excluding them, we find that the CFP for CLASH is fully compatible with the simulation results with The Three Hundred project clusters. This result suggests the possibility that the inclusion of clusters undergoing mergers (Ricker & Sarazin 2001; Rasia et al. 2011) can significantly affect the inference of the CFP parameters.

Moreover, we explored potential sources of systematic effects that could potentially bias the determination of the CFP, such as the NFW fitting procedure and the effects of the $\sigma_{\rm fit}$ selection (Section 8). We conclude that all the results presented in this paper are robust against these effects. Moreover, we confront our results with the CFP obtained for other cosmological cluster simulations, finding that the overall trends are consistent with our findings from The Three Hundred project simulations.

This study has been centred on massive haloes (all clusters having $T > 2.5$ keV and the average temperature of the sample exceeding 5 keV) which for the hierarchical structure formation model are the latest objects to form. As a result, the entire sample includes mostly unrelaxed clusters at all redshifts. Despite this condition, we always find that the CFP is extremely well defined with a low dispersion around the plane ($\sigma_d < 0.03$ dex). Even restricting the analysis to only the most disturbed systems or the most recently formed objects, the dispersion remains low. We expect that the reduced dispersion not only holds but even improves when including lower mass systems that are not probed in this work, because smaller objects form earlier on average and are thus more relaxed. Thus far, the CFP has been directly

---

[3] However, we reiterate again that for the larger aperture radii of r_{500} and r_{200}, there is a substantial aperture mismatch with respect to the characteristic scale radius r_s of haloes.

measured only for the CLASH sample, which is quite unique for its characteristics and is also composed of extremely massive objects. Therefore, it would be interesting to extend the analysis to cluster samples with a wider mass range as targeted by ongoing cluster programmes, such as the CHEX-MATE programme (CHEX-MATE Collaboration et al. 2021), the XXL X-ray survey (Pierre et al. 2016), and the eROSITA X-ray survey (Brunner et al. 2021), as well as blind Sunyaev–Zel'dovich effect surveys (e.g. Hilton et al. 2021) and optical and near-infrared imaging surveys (e.g. Rubin Observatory LSST, *Euclid*, and *Nancy Grace Roman Space Telescope* missions).

DATA AVAILABILITY

The data used in this paper are part of The Three Hundred project collaboration and can be accessed following the guidelines in the main website[4] of the project.

REFERENCES

Bartelmann M., Steinmetz M., 1996, MNRAS, 283, 431
Beck A. M. et al., 2016, MNRAS, 455, 2110
Bertschinger E., 1985, ApJS, 58, 39
Blandford R. D., Narayan R., 1992, ARA&A, 30, 311
Brunner H. et al., 2021, A&A, preprint (arXiv:2106.14517)
Chabrier G., 2003, PASP, 115, 763
CHEX-MATE Collaboration et al., 2021, A&A, 650, A104
Child H. L., Habib S., Heitmann K., Frontiere N., Finkel H., Pope A., Morozov V., 2018, ApJ, 859, 55

Cui W., Power C., Borgani S., Knebe A., Lewis G. F., Murante G., Poole G. B., 2017, MNRAS, 464, 2502
Cui W. et al., 2018, MNRAS, 480, 2898
De Luca F., De Petris M., Yepes G., Cui W., Knebe A., Rasia E., 2021, MNRAS, 504, 5383
Diemer B., More S., Kravtsov A. V., 2013, ApJ, 766, 25
Donahue M. et al., 2014, ApJ, 794, 136
Foreman-Mackey D., 2016, J. Open Source Softw., 1, 24
Frenk C. S., White S. D. M., Efstathiou G., Davis M., 1990, ApJ, 351, 10
Fujita Y., Umetsu K., Rasia E., Meneghetti M., Donahue M., Medezinski E., Okabe N., Postman M., 2018a, ApJ, 857, 118
Fujita Y., Umetsu K., Ettori S., Rasia E., Okabe N., Meneghetti M., 2018b, ApJ, 863, 37
Haardt F., Madau P., 1996, ApJ, 461, 20
Haggar R., Gray M. E., Pearce F. R., Knebe A., Cui W., Mostoghiu R., Yepes G., 2020, MNRAS, 492, 6074
Harris C. R. et al., 2020, Nature, 585, 357
Hennawi J. F., Dalal N., Bode P., Ostriker J. P., 2007, ApJ, 654, 714
Hilton M. et al., 2021, ApJS, 253, 3
Hunter J. D., 2007, Comput. Sci. Eng., 9, 90
Jenkins A., Frenk C. S., White S. D. M., Colberg J. M., Cole S., Evrard A. E., Couchman H. M. P., Yoshida N., 2001, MNRAS, 321, 372
Kang H., Cen R., Ostriker J. P., Ryu D., 1994, ApJ, 428, 1
Klypin A., Yepes G., Gottlöber S., Prada F., Heß S., 2016, MNRAS, 457, 4340
Knollmann S. R., Knebe A., 2009, ApJS, 182, 608
Ludlow A. D. et al., 2013, MNRAS, 432, 1103
Markevitch M., 1998, ApJ, 504, 27
Mathiesen B. F., Evrard A. E., 2001, ApJ, 546, 100
Maughan B. J., Jones C., Forman W., Van Speybroeck L., 2008, ApJS, 174, 117
Mazzotta P., Rasia E., Moscardini L., Tormen G., 2004, MNRAS, 354, 10
Meneghetti M., Fedeli C., Pace F., Gottlöber S., Yepes G., 2010, A&A, 519, A90
Meneghetti M. et al., 2014, ApJ, 797, 34
Meneghetti M. et al., 2020, Science, 369, 1347
Merritt D., Graham A. W., Moore B., Diemand J., Terzić B., 2006, AJ, 132, 2685
Merten J. et al., 2015, ApJ, 806, 4
Mostoghiu R., Knebe A., Cui W., Pearce F. R., Yepes G., Power C., Dave R., Arth A., 2019, MNRAS, 483, 3390
Navarro J. F., Frenk C. S., White S. D. M., 1996, ApJ, 462, 563
Navarro J. F., Frenk C. S., White S. D. M., 1997, ApJ, 490, 493
Navarro J. F. et al., 2004, MNRAS, 349, 1039
Oguri M., Blandford R. D., 2009, MNRAS, 392, 930
Pierre M. et al., 2016, A&A, 592, A1
Planck Collaboration, 2013, A&A, 550, A131
Planck Collaboration, 2016, A&A, 594, A13
Planelles S. et al., 2017, MNRAS, 467, 3827
Postman M. et al., 2012, ApJS, 199, 25
Rasia E., Mazzotta P., Evrard A., Markevitch M., Dolag K., Meneghetti M., 2011, ApJ, 729, 45
Rasia E. et al., 2015, ApJ, 813, L17
Reiprich T. H., Böhringer H., 2002, ApJ, 567, 716
Ricker P. M., Sarazin C. L., 2001, ApJ, 561, 621
Schaller M. et al., 2015, MNRAS, 452, 343
Schmidt R. W., Allen S. W., 2007, MNRAS, 379, 209
Springel V., 2005, MNRAS, 364, 1105
Springel V., Hernquist L., 2003, MNRAS, 339, 289
Steinborn L. K., Dolag K., Hirschmann M., Prieto M. A., Remus R.-S., 2015, MNRAS, 448, 1504
Tornatore L., Borgani S., Dolag K., Matteucci F., 2007, MNRAS, 382, 1050
Torri E., Meneghetti M., Bartelmann M., Moscardini L., Rasia E., Tormen G., 2004, MNRAS, 349, 476
Umetsu K., 2020, A&AR, 28, 7
Umetsu K. et al., 2009, ApJ, 694, 1643
Umetsu K. et al., 2014, ApJ, 795, 163

Umetsu K., Zitrin A., Gruen D., Merten J., Donahue M., Postman M., 2016, ApJ, 821, 116

Vikhlinin A., Kravtsov A., Forman W., Jones C., Markevitch M., Murray S. S., Van Speybroeck L., 2006, ApJ, 640, 691

Wechsler R. H., Bullock J. S., Primack J. R., Kravtsov A. V., Dekel A., 2002, ApJ, 568, 52

White S. D. M., Efstathiou G., Frenk C. S., 1993, MNRAS, 262, 1023

Wiersma R. P. C., Schaye J., Smith B. D., 2009, MNRAS, 393, 99

Zhao D. H., Mo H. J., Jing Y. P., Börner G., 2003, MNRAS, 339, 12

Zitrin A. et al., 2015, ApJ, 801, 44

APPENDIX A: PARAMETERS DEFINING THE CFP

In this appendix, we summarize the parameters defining the CFP and its thickness for The Three Hundred project clusters determined at different redshifts and with different temperature definitions (Table A1), and those obtained for the relaxed and unrelaxed subsamples at $z = 0$ (Table A2), and those at $z = 0$ for subsamples with different formation redshifts (Table A3).

Table A1. Best-fitting parameters (α, β, and δ) and thickness (σ_d in dex units) of the Fundamental Plane obtained for The Three Hundred project clusters at different redshifts and with different temperature definitions. The results are obtained from NFW fits to the centre-excised mass profile inside r_{200}. For each redshift, the number of clusters and the median values of the characteristic scale parameters, $r_{s,0}$ and $M_{s,0}$, are listed at the bottom of each panel. For each quantity, the upper and lower errors enclose the 1σ uncertainty. The dashes correspond to δ errors smaller than 5×10^{-4}.

$z = 0.07$	α	β	δ	σ_d	T_0
$T_{\mathrm{mw}}(500\,h^{-1}\,\mathrm{kpc})$	$1.18^{+0.03}_{-0.03}$	$-1.30^{+0.04}_{-0.04}$	0.000^{-}_{-}	0.017	6.35
$T_{\mathrm{mw}}(r_{500})$	$1.06^{+0.02}_{-0.02}$	$-1.18^{+0.03}_{-0.03}$	0.000^{-}_{-}	0.016	5.67
$T_{\mathrm{mw}}(r_{200})$	$1.03^{+0.02}_{-0.02}$	$-1.13^{+0.03}_{-0.03}$	0.000^{-}_{-}	0.015	5.05
$T_{\mathrm{sl}}(500\,h^{-1}\,\mathrm{kpc})$	$1.23^{+0.05}_{-0.04}$	$-1.47^{+0.06}_{-0.07}$	0.000^{-}_{-}	0.022	5.97
$T_{\mathrm{sl}}(r_{500})$	$1.21^{+0.04}_{-0.03}$	$-1.52^{+0.05}_{-0.06}$	$0.016^{+0.003}_{-0.003}$	0.019	5.54
$T_{\mathrm{sl}}(r_{200})$	$1.23^{+0.04}_{-0.03}$	$-1.56^{+0.05}_{-0.05}$	$0.014^{+0.003}_{-0.003}$	0.018	5.32
Number = 231		$M_{s,0} = 1.65 \times 10^{14}\,h^{-1}\,\mathrm{M_\odot}$		$r_{s,0} = 329\,h^{-1}\,\mathrm{kpc}$	
$z = 0.22$	α	β	δ	σ_d	T_0
$T_{\mathrm{mw}}(500\,h^{-1}\,\mathrm{kpc})$	$1.10^{+0.02}_{-0.02}$	$-1.23^{+0.03}_{-0.03}$	0.000^{-}_{-}	0.016	5.45
$T_{\mathrm{mw}}(r_{500})$	$1.00^{+0.02}_{-0.02}$	$-1.12^{+0.03}_{-0.03}$	$0.007^{+0.002}_{-0.002}$	0.018	4.93
$T_{\mathrm{mw}}(r_{200})$	$0.97^{+0.02}_{-0.02}$	$-1.06^{+0.03}_{-0.03}$	0.000^{-}_{-}	0.018	4.44
$T_{\mathrm{sl}}(500\,h^{-1}\,\mathrm{kpc})$	$1.13^{+0.03}_{-0.03}$	$-1.35^{+0.04}_{-0.05}$	0.000^{-}_{-}	0.020	5.13
$T_{\mathrm{sl}}(r_{500})$	$1.08^{+0.03}_{-0.02}$	$-1.34^{+0.04}_{-0.04}$	0.000^{-}_{-}	0.018	4.86
$T_{\mathrm{sl}}(r_{200})$	$1.12^{+0.03}_{-0.02}$	$-1.41^{+0.04}_{-0.04}$	$0.002^{+0.003}_{-0.003}$	0.019	4.70
Number = 243		$M_{s,0} = 1.34 \times 10^{14}\,h^{-1}\,\mathrm{M_\odot}$		$r_{s,0} = 303\,h^{-1}\,\mathrm{kpc}$	
$z = 0.33$	α	β	δ	σ_d	T_0
$T_{\mathrm{mw}}(500\,h^{-1}\,\mathrm{kpc})$	$1.10^{+0.02}_{-0.02}$	$-1.26^{+0.03}_{-0.03}$	$-0.005^{+0.002}_{-0.002}$	0.015	5.09
$T_{\mathrm{mw}}(r_{500})$	$1.00^{+0.01}_{-0.02}$	$-1.13^{+0.03}_{-0.02}$	$-0.011^{+0.002}_{-0.002}$	0.017	4.73
$T_{\mathrm{mw}}(r_{200})$	$0.98^{+0.02}_{-0.02}$	$-1.07^{+0.03}_{-0.03}$	$-0.006^{+0.002}_{-0.002}$	0.018	4.18
$T_{\mathrm{sl}}(500\,h^{-1}\,\mathrm{kpc})$	$1.11^{+0.02}_{-0.02}$	$-1.37^{+0.04}_{-0.04}$	$0.001^{+0.003}_{-0.003}$	0.019	4.79
$T_{\mathrm{sl}}(r_{500})$	$1.06^{+0.02}_{-0.02}$	$-1.32^{+0.03}_{-0.04}$	$-0.009^{+0.002}_{-0.002}$	0.018	4.65
$T_{\mathrm{sl}}(r_{200})$	$1.09^{+0.02}_{-0.02}$	$-1.36^{+0.04}_{-0.04}$	$0.000^{+0.000}_{-0.000}$	0.018	4.49
Number = 243		$M_{s,0} = 1.18 \times 10^{14}\,h^{-1}\,\mathrm{M_\odot}$		$r_{s,0} = 288\,h^{-1}\,\mathrm{kpc}$	
$z = 0.59$	α	β	δ	σ_d	T_0
$T_{\mathrm{mw}}(500\,h^{-1}\,\mathrm{kpc})$	$1.10^{+0.02}_{-0.02}$	$-1.23^{+0.03}_{-0.03}$	0.000^{-}_{-}	0.017	4.15
$T_{\mathrm{mw}}(r_{500})$	$0.98^{+0.02}_{-0.02}$	$-1.10^{+0.03}_{-0.03}$	0.000^{-}_{-}	0.019	3.96
$T_{\mathrm{mw}}(r_{200})$	$0.95^{+0.02}_{-0.02}$	$-1.04^{+0.03}_{-0.03}$	0.000^{-}_{-}	0.019	3.54
$T_{\mathrm{sl}}(500\,h^{-1}\,\mathrm{kpc})$	$1.09^{+0.02}_{-0.02}$	$-1.34^{+0.04}_{-0.04}$	0.000^{-}_{-}	0.019	4.04
$T_{\mathrm{sl}}(r_{500})$	$1.03^{+0.02}_{-0.02}$	$-1.28^{+0.04}_{-0.03}$	0.000^{-}_{-}	0.018	3.90
$T_{\mathrm{sl}}(r_{200})$	$1.05^{+0.02}_{-0.02}$	$-1.31^{+0.04}_{-0.04}$	$0.006^{+0.002}_{-0.002}$	0.019	3.77
Number = 274		$M_{s,0} = 8.54 \times 10^{13}\,h^{-1}\,\mathrm{M_\odot}$		$r_{s,0} = 239\,h^{-1}\,\mathrm{kpc}$	
$z = 0.99$	α	β	δ	σ_d	T_0
$T_{\mathrm{mw}}(500\,h^{-1}\,\mathrm{kpc})$	$1.08^{+0.01}_{-0.02}$	$-1.17^{+0.03}_{-0.03}$	0.000^{-}_{-}	0.017	2.93
$T_{\mathrm{mw}}(r_{500})$	$0.94^{+0.01}_{-0.02}$	$-1.04^{+0.03}_{-0.03}$	0.000^{-}_{-}	0.016	3.10
$T_{\mathrm{mw}}(r_{200})$	$0.94^{+0.02}_{-0.01}$	$-1.01^{+0.03}_{-0.03}$	0.000^{-}_{-}	0.016	2.72
$T_{\mathrm{sl}}(500\,h^{-1}\,\mathrm{kpc})$	$1.03^{+0.02}_{-0.02}$	$-1.24^{+0.03}_{-0.03}$	0.000^{-}_{-}	0.017	3.06
$T_{\mathrm{sl}}(r_{500})$	$0.95^{+0.02}_{-0.02}$	$-1.15^{+0.03}_{-0.03}$	0.000^{-}_{-}	0.019	3.10
$T_{\mathrm{sl}}(r_{200})$	$0.97^{+0.02}_{-0.02}$	$-1.19^{+0.04}_{-0.03}$	$0.000^{+0.002}_{-0.002}$	0.018	2.98
Number = 280		$M_{s,0} = 5.19 \times 10^{13}\,h^{-1}\,\mathrm{M_\odot}$		$r_{s,0} = 185\,h^{-1}\,\mathrm{kpc}$	

Table A2. Same as Table 2, but for the relaxed ($\chi_{DS} \geq 1$, upper panel) and unrelaxed ($\chi_{DS} \leq 2/3$, lower panel) subsamples at $z = 0$.

	α	β	δ	σ_d (dex)	T_0 (keV)
$T_{mw}(500\,h^{-1}\,\mathrm{kpc})$	$1.01^{+0.05}_{-0.04}$	$-0.99^{+0.07}_{-0.08}$	$-0.003^{+0.003}_{-0.003}$	0.018	6.71
$T_{mw}(r_{500})$	$0.96^{+0.04}_{-0.03}$	$-1.02^{+0.05}_{-0.06}$	$0.001^{+0.002}_{-0.002}$	0.013	5.53
$T_{mw}(r_{200})$	$0.91^{+0.04}_{-0.03}$	$-0.94^{+0.04}_{-0.05}$	$0.005^{+0.002}_{-0.002}$	0.012	4.94
$T_{sl}(500\,h^{-1}\,\mathrm{kpc})$	$1.07^{+0.08}_{-0.05}$	$-1.15^{+0.10}_{-0.11}$	$-0.009^{+0.005}_{-0.005}$	0.026	6.53
$T_{sl}(r_{500})$	$1.05^{+0.06}_{-0.04}$	$-1.23^{+0.07}_{-0.08}$	$-0.007^{+0.003}_{-0.004}$	0.016	5.80
$T_{sl}(r_{200})$	$1.06^{+0.06}_{-0.04}$	$-1.27^{+0.07}_{-0.08}$	$-0.013^{+0.003}_{-0.004}$	0.015	5.68
Number = 90		$M_{s,0} = 1.67 \times 10^{14}\,h^{-1}\,\mathrm{M_\odot}$		$r_{s,0} = 355\,h^{-1}\,\mathrm{kpc}$	
	α	β	δ	σ_d (dex)	T_0 (keV)
$T_{mw}(500\,h^{-1}\,\mathrm{kpc})$	$1.20^{+0.13}_{-0.09}$	$-1.50^{+0.11}_{-0.12}$	$-0.004^{+0.007}_{-0.007}$	0.022	6.63
$T_{mw}(r_{500})$	$1.02^{+0.07}_{-0.05}$	$-1.15^{+0.07}_{-0.07}$	$-0.008^{+0.004}_{-0.004}$	0.019	5.71
$T_{mw}(r_{200})$	$1.00^{+0.05}_{-0.03}$	$-1.08^{+0.06}_{-0.06}$	$-0.006^{+0.004}_{-0.004}$	0.024	5.09
$T_{sl}(500\,h^{-1}\,\mathrm{kpc})$	$1.40^{+0.22}_{-0.15}$	$-1.71^{+0.16}_{-0.18}$	$-0.019^{+0.009}_{-0.010}$	0.031	6.04
$T_{sl}(r_{500})$	$1.16^{+0.14}_{-0.09}$	$-1.44^{+0.12}_{-0.12}$	$-0.002^{+0.006}_{-0.007}$	0.023	5.25
$T_{sl}(r_{200})$	$1.20^{+0.13}_{-0.08}$	$-1.50^{+0.11}_{-0.12}$	$-0.004^{+0.007}_{-0.007}$	0.026	4.96
Number = 87		$M_{s,0} = 2.49 \times 10^{14}\,h^{-1}\,\mathrm{M_\odot}$		$r_{s,0} = 513\,h^{-1}\,\mathrm{kpc}$	

Table A3. Same as Table 2, but for The Three Hundred project clusters at $z = 0$ with different formation redshifts: $z_{\rm form} < 0.4$, $0.4 \leq z_{\rm form} < 0.6$, and $z_{\rm form} \geq 0.6$.

$z_{\rm form} \geq 0.6$	α	β	δ	$\sigma_{\rm d}$ (dex)	T_0 (keV)
$T_{\rm mw}(500\,h^{-1}\,{\rm kpc})$	$1.04^{+0.04}_{-0.03}$	$-1.09^{+0.06}_{-0.07}$	$0.013^{+0.004}_{-0.004}$	0.021	6.71
$T_{\rm mw}(r_{500})$	$0.98^{+0.03}_{-0.03}$	$-1.05^{+0.05}_{-0.05}$	$0.017^{+0.002}_{-0.002}$	0.012	5.68
$T_{\rm mw}(r_{200})$	$0.92^{+0.04}_{-0.03}$	$-0.94^{+0.05}_{-0.05}$	$0.018^{+0.002}_{-0.002}$	0.012	5.07
$T_{\rm sl}(500\,h^{-1}\,{\rm kpc})$	$1.11^{+0.07}_{-0.05}$	$-1.27^{+0.10}_{-0.11}$	$0.018^{+0.006}_{-0.006}$	0.022	6.42
$T_{\rm sl}(r_{500})$	$1.10^{+0.05}_{-0.04}$	$-1.33^{+0.07}_{-0.08}$	$0.019^{+0.004}_{-0.004}$	0.017	5.82
$T_{\rm sl}(r_{200})$	$1.10^{+0.05}_{-0.04}$	$-1.37^{+0.07}_{-0.09}$	$0.013^{+0.004}_{-0.004}$	0.017	5.69
Number = 87		$M_{\rm s,0} = 1.66 \times 10^{14}\,h^{-1}\,{\rm M}_\odot$		$r_{\rm s,0} = 336\,h^{-1}\,{\rm kpc}$	
$0.4 \leq z_{\rm form} < 0.6$	α	β	δ	$\sigma_{\rm d}$ (dex)	T_0 (keV)
$T_{\rm mw}(500\,h^{-1}\,{\rm kpc})$	$1.03^{+0.07}_{-0.05}$	$-1.08^{+0.08}_{-0.09}$	$-0.021^{+0.005}_{-0.004}$	0.019	6.97
$T_{\rm mw}(r_{500})$	$0.91^{+0.03}_{-0.03}$	$-0.91^{+0.05}_{-0.06}$	$-0.002^{+0.003}_{-0.003}$	0.013	5.58
$T_{\rm mw}(r_{200})$	$0.91^{+0.02}_{-0.02}$	$-0.89^{+0.05}_{-0.05}$	$0.000^{+0.003}_{-0.003}$	0.012	4.95
$T_{\rm sl}(500\,h^{-1}\,{\rm kpc})$	$1.14^{+0.11}_{-0.08}$	$-1.41^{+0.13}_{-0.15}$	$-0.020^{+0.007}_{-0.008}$	0.028	6.42
$T_{\rm sl}(r_{500})$	$0.99^{+0.06}_{-0.04}$	$-1.15^{+0.07}_{-0.07}$	$0.000^{+0.004}_{-0.004}$	0.016	5.48
$T_{\rm sl}(r_{200})$	$1.06^{+0.07}_{-0.05}$	$-1.32^{+0.10}_{-0.11}$	$0.000^{+0.005}_{-0.006}$	0.017	5.16
Number = 75		$M_{\rm s,0} = 2.02 \times 10^{14}\,h^{-1}\,{\rm M}_\odot$		$r_{\rm s,0} = 431\,h^{-1}\,{\rm kpc}$	
$z_{\rm form} < 0.4$	α	β	δ	$\sigma_{\rm d}$ (dex)	T_0 (keV)
$T_{\rm mw}(500\,h^{-1}\,{\rm kpc})$	$1.27^{+0.06}_{-0.05}$	$-1.46^{+0.07}_{-0.08}$	$-0.002^{+0.005}_{-0.005}$	0.021	6.55
$T_{\rm mw}(r_{500})$	$1.11^{+0.04}_{-0.04}$	$-1.21^{+0.06}_{-0.06}$	$-0.016^{+0.004}_{-0.004}$	0.017	5.61
$T_{\rm mw}(r_{200})$	$1.06^{+0.04}_{-0.03}$	$-1.12^{+0.06}_{-0.06}$	$-0.016^{+0.004}_{-0.004}$	0.020	5.07
$T_{\rm sl}(500\,h^{-1}\,{\rm kpc})$	$1.55^{+0.13}_{-0.10}$	$-1.80^{+0.13}_{-0.16}$	$-0.029^{+0.009}_{-0.009}$	0.034	6.03
$T_{\rm sl}(r_{500})$	$1.26^{+0.07}_{-0.06}$	$-1.49^{+0.08}_{-0.08}$	$-0.007^{+0.006}_{-0.006}$	0.020	5.16
$T_{\rm sl}(r_{200})$	$1.25^{+0.06}_{-0.05}$	$-1.51^{+0.07}_{-0.08}$	$-0.016^{+0.005}_{-0.005}$	0.020	5.01
Number = 83		$M_{\rm s,0} = 2.49 \times 10^{14}\,h^{-1}\,{\rm M}_\odot$		$r_{\rm s,0} = 518\,h^{-1}\,{\rm kpc}$	

This paper has been typeset from a TeX/LaTeX file prepared by the author.